Renewable Energy 176 (2021) 617–634

Contents lists available at ScienceDirect

Renewable Energy

journal homepage: www.elsevier.com/locate/renene

Experimental investigation of a building-integrated, transparent, concentrating photovoltaic and thermal collector

Nick Novelli [d, *], Kenton Phillips [a, 1], Justin Shultz [a, 2], Melanie M. Derby [c], Ryan Salvas [a], Jesse Craft [b], Peter Stark [a, 3], Michael Jensen [b], Stephen Derby [b], Anna Dyson [d]

[a] Center for Architecture Science and Ecology, Rensselaer Polytechnic Institute, 110 8th Street, Troy, NY, 12180, USA
[b] Department of Mechanical, Aerospace and Nuclear Engineering, Rensselaer Polytechnic Institute, 110 8th Street, Troy, NY, 12180, USA
[c] Department of Mechanical and Nuclear Engineering, Kansas State University, Manhattan, KS, 66506, USA
[d] Yale Center for Ecosystems in Architecture, Yale University, 180 York Street, New Haven, CT 06511, USA

ARTICLE INFO

Article history:
Received 24 November 2020
Received in revised form
14 April 2021
Accepted 7 May 2021
Available online 17 May 2021

Keywords:
Net-zero buildings
Energy-positive buildings
Active integrated façades
Solar cogeneration
Building-integrated concentrating photovoltaics
Dynamic glazing systems

ABSTRACT

As buildings consume roughly one-third of global primary energy, more effective strategies are required to convert on-site solar energy. Here, a multifunctional building façade system, using less than 1% of the semiconductor materials of conventional systems, was tested and developed to expand opportunities for net-zero commercial architecture by synergistically reducing cooling loads, lighting loads, and contributions to urban heat island effects, while converting ambient solar energy resources for internal demands. The **B**uilding **I**ntegrated, **T**ransparent, **C**oncentrating, **P**hotovoltaic and **T**hermal collector (BITCoPT) optically separates diffuse and direct irradiance, transmitting diffuse light for illumination and views. Here, direct irradiance (which is often rejected in commercial buildings to control glare and cooling loads) is intercepted by BITCoPT and converted into electricity and thermal energy. A prototype was tested, demonstrating 43.6% cogeneration efficiency (at a 58 °C operating temperature) relative to direct normal irradiance transmitted through the building's exterior glazing, and 39.0% at 70 °C (which could supply active thermal processes at nominal coefficients of performance). An analytical model was calibrated with observed data, showing good correlation. By substituting parameter values for projected upgrades (to optics, cell type and exterior glazing) into the BITCoPT model, simulated cogeneration efficiency increased to 71.2% at 70 °C (31.2% electrical, 40.0% thermal).

1. Introduction: Building-integrated solar harvesting

Reducing the fossil fuel consumption of buildings is critical towards improving the resiliency of our planetary environment, as over one-third of current primary energy use is in the non-industrial building sector [1,2]. Prior approaches towards reforming the built environment process have had limited success in achieving sustainable development targets set by the United Nations [3] and others, in part because advances in renewable energy systems have not been adequately integrated into the balance of the building's systems, resulting in inefficient and disaggregated environmental controls. Furthermore, solar collection devices have not reached the necessary efficiencies to justify covering areas with opaque, single-function panels onto surfaces that are typically prioritized for glazing. Because solar energy is a potentially multifaceted resource, here, a multifunctional approach was investigated, whereby the various potentials of solar flux are matched with both aesthetic and functional building requirements towards improved net energy use, and energy consumption, at the whole-building scale [4].

Currently, energy delivered to buildings sites from primary sources is predominantly supplied in the form of high-grade carriers such as electricity and hydrocarbon fuels. However, the service demands of the built environment—such as lighting, heating, cooling, ventilation, humidity control and human health and well-

* Corresponding author.
E-mail addresses: nick.novelli@outlook.com (N. Novelli), kenton.phillips@burohappold.com (K. Phillips), jshultz@eypae.com (J. Shultz), derbym@ksu.edu (M.M. Derby), ryan.salvas@gmail.com (R. Salvas), craftj2@gmail.com (J. Craft), prhstark@seas.harvard.edu (P. Stark), jensenmk@gmail.com (M. Jensen), sderby1@gmail.com (S. Derby), anna.dyson@yale.edu (A. Dyson).
[1] Current address: Buro Happold, 100 Broadway #23, New York, NY 10005, USA.
[2] Current address: EYP Architecture & Engineering, 1000 Potomac St NW #L1, Washington, DC 20007.
[3] Current address: School of Engineering and Applied Science, Harvard University, 18 Oxford St, Cambridge, MA 02138, USA.

https://doi.org/10.1016/j.renene.2021.05.046
0960-1481/

Nomenclature

Variables

A	area (m^2)
c_{scatt}	coefficient of optical scattering (dimensionless)
c_p	specific heat (kJ/kg-K)
E	electricity (W)
F	fraction of area ratio (dimensionless)
G	solar power (W)
I	solar irradiance (W/m^2) or electrical current (A)
k	conduction heat transfer coefficient (W/m-K), or scaling constant
n	index of refraction, or count (dimensionless)
Q	thermal power (W)
R	thermal resistance (K/W), or reflectance (dimensionless)
T	temperature (°C, K), or optical transmittance (dimensionless)
U	overall heat transfer coefficient (W/m^2-K)
V	volumetric flow rate (m^3/s)
V	electrical potential (V)
x	glazing lite thickness (m)
X	concentration ratio (dimensionless)

Greek letters

η	energy collection efficiency (dimensionless)
θ	angle of incidence (degrees)
ρ	density (kg/m^3)

Subscripts and Abbreviations

AIF	active integrated façade
AOI	angle of incidence
BIPV	building-integrated photovoltaic
BIPVT	building-integrated photovoltaic and solar thermal
BITCoPT	building-integrated transparent concentrating photovoltaic and thermal solar collector
cav	cavity
cogen	cogeneration (electrical and thermal collection)
CPV	concentrator photovoltaic cell
DN	direct normal solar irradiance
FF	fill factor
Fres	Fresnel (reflectance)
gen	generation or collection
glaz	glazing
homo	homogeneous shading condition and cogeneration status (of a set of modules)
hetero	heterogeneous shading condition and cogeneration status (of a set of modules)
HTF	heat transfer fluid
lite	lite (glazing)
OC	open circuit (voltage)
opt	concentrator optics
POE	primary optical element
proj	projected model configuration
proto	operational prototype model configuration
PV	photovoltaic
SC	short circuit (current)
sfc	surface
SA	sub-array of BITCoPT modules
SOE	secondary optical element
WBHX	water block heat exchanger

being factors—could potentially be met with distributed, lower grade climatic energy resources that are available on-site. A multifaceted, system-of-systems design approach would coordinate and couple the specific characteristics and mechanisms (rather than simply the quantities) of both the resources, and the service demands.

A multifaceted approach to harvesting on-site solar energy (insolation) for building use is investigated in this study because solar energy is both plentiful in the built environment and currently under-utilized [5]. Through fenestration strategies, available insolation is transformed simultaneously into electricity, thermal energy, and luminance. Moreover, in commercial buildings, it is often beneficial to limit solar gains, because there exist other large daytime heat sources (such as equipment and people) which create significant cooling demands. Addressing these multiple factors together might therefore expand the opportunities for net-zero and energy-positive building projects.

Insolation is available as diffuse and direct normal irradiance, and both forms can be utilized to meet building service demands. Daylight is advantageous for lighting indoors, as it naturally: contributes to circadian entrainment (encouraging wakefulness [6]); contributes to occupant satisfaction [7] and increased property value [8]; and is implicated in other health and performance therapies, including treatment of various depressions [9]. A baseline diffuse luminous environment is generally desirable in commercial office settings, so diffuse sunlight is potentially a cost-effective method of providing sufficient (but not excess) illumination to a portion of the occupied floorplate, as gauged by a metric such as Useful Daylighting Illuminance [10]. Conversely, the direct normal component of irradiance (I_{DN}) has a lower average luminous efficacy than the diffuse component [11], and due to its directionality and intensity, often needs to be modified by the fenestration to be useful as indoor light without causing undue glare and thermal gains, in cooling-dominated contexts and in certain building types such as offices and classrooms where high contrast lighting is undesirable. Direct irradiance can, however, be converted to electricity with photovoltaics (PV) and captured as thermal energy with appropriate heat exchangers. Additionally, if I_{DN} is concentrated, then it can be collected as thermal energy at temperatures high enough to not-only provide heating, but also to drive heat engines, thereby increasing the efficiency of the building's systems overall.

Beyond performance benefits, building-integrated solar concentration has potential life-cycle analysis (LCA) benefits over non-concentrating PV: Optical concentrating collectors employ small-format semiconductor photovoltaics in concert with fixturing and optics constructed of abundant and recyclable materials (glass, metal, plastic), rather than the relatively high amount of semiconductor material in conventional flat plate PV collectors. Largely through the several-hundred-fold reduction in semiconductor material, grid-scale concentrating solar systems were found to improve in carbon dioxide emissions equivalence and energy payback relative to mono-silicon PV, and to approach CdTe panel technology values, with that technology's highly developed material efficiency and supply chain [12].

Compounding the LCA benefits of these concentrating modules, integration with other building systems adds further LCA and material benefits. Because the building provides structural support, by integrating tracking PV into a building's fenestration, less marginal

structural rigidity is required than for stand-alone concentrating systems. Types of building-integrated concentrating systems have been found to be materially and life-cycle efficient relative to non-concentrating systems [13]. Additionally, an LCA performed on a housing unit with a prototype concentrating skylight concluded the technology had a positive carbon balance relative to de-carbonizing grid mixes, and baseline photovoltaics, even in a sub-optimal (small, residential) program, suggesting potential on-going benefits in evolving large-scale energy systems applications [14].

1.1. Precedents and related work: Studies and technologies for high-efficiency building-integrated Photovoltaic and Thermal (BIPVT) systems

Active Integrated Façade (AIF) technologies have consistently been identified as potentially enabling for building self-sufficiency [15,16]. In particular, shading systems, solar collecting AIFs (AIF-SCs), Building-Integrated Photovoltaics (BIPV), solar thermal and BIPV with thermal collection (BIST and BIPVT), and concentrating AIF-SCs are noted here as related technologies to the concept studied. The ongoing development of material-scale glazing enhancements, both dynamic [17], and static [18,19], has potential for AIF development as well, though this study focuses on device-scale systems.

Dynamic shading systems such as motorized blinds or louvers are gaining increasing commercial adoption for the mitigation of undesired solar gains and even distribution of daylight throughout an occupied space [20]. However, because their effectiveness at reducing solar gain correlates to their opacity, active shading devices often compromise between energy performance and desirable daylighting and views to the exterior [21]. As such, these systems can have difficulty reducing glare to acceptable levels [22]. Due to the relative maturity of these motorized shading products, research is active on their system parameters, and in particular, control strategies [23]. But while active shading systems can reduce energy demand, if they harvest on-site energy, they use conventional BIPV which does not adequately supply the range of electrical and hot water demands as required for on-site net-zero and energy-positive buildings.

Solar-collecting AIFs (such as photovoltaic cladding, or laminated, semi-transparent PV) collect and transform some insolation, but despite their multiple society-wide benefits [24], their adoption is yet limited, perhaps due (in part) to their being optimized towards energy collection [25,26], which limits their potential for return on investment, and results in compromises on other primary envelope performance criteria. Building-Integrated PV fenestration (BIPV) has long been investigated [27,28] and shows some commercial uptake [29]. Fenestration is responsible for visual indoor-outdoor connections, daylighting and management of heat and moisture, and are the result of a multi-variate tradeoff process [30,31]. Although BIPV power generation can be substantial, the energy collection of an AIF-SC should support and even enhance other criteria (Fig. 1), to encourage uptake.

BIPVs (similar to dynamic shading systems) are limited by the tradeoff with the daylighting criteria of a building's fenestration [32]. And although BIPV has been shown to reduce cooling loads [33], energy generated can be outweighed by increased cooling loads if the resultant envelope's heat transfer characteristics are not appropriate [34], and conversely can poorly insulate against heat loss in cold-climate conditions [35]. This apparent paradox highlights the need to integrate AIF design with the balance of a building's systems.

To increase the utility of solar energy, combining BIPV with thermal collection (cogeneration, or BIPVT) has been explored in modelling and experimentation [36–39]. On-site thermal collection is attractive thermodynamically, because it can offset heat that would otherwise be supplied by high exergy-destruction processes, namely fuel combustion (on-site, in boilers, or remote, in power plants, for resistance heating). In simulation, BIPVT provides higher combined efficiency than deploying only PV, thermal collection, or a mixture of the two types [40,41]. Integrating a cogeneration technology directly into a building's envelope is shown to contribute value in some cases [42]. Like BIPV, these systems can be semi-transparent (BISPVT), and can demonstrate efficiency benefits alongside daylighting [43,44], albeit with similar tradeoffs between areas for harvesting energy and areas for daylighting and views [45]. Although exergetic efficiency of collection increases with operating temperature (assuming losses can be limited), BIPVT studies (with some exceptions such as [46]) largely focus on reducing PV cell temperatures (maintaining electrical efficiency) and channeling the collected low-grade heat for either direct use or for subsequent boosting in quality via heat pumps [46].

To increase collection efficiency and address the compromises of BIPV or building integrated solar thermal systems (between desiring daylighting and preservation of views to the exterior) concentrating and selective AIF-SCs have been explored [47]. Concentrating AIF-SCs redirect and intensify incident insolation, either with mirrors [48–50], lenses [51–58] or with spectrally selective surfaces [59,60] so that daylighting and/or views can be provided along with power generation, and in some cases with high-temperature collection, potentially increasing the efficiency of cogeneration schemes [61]. In this context “high temperature” refers to 50 °C and higher, which could drive scalable sorption chilling processes at COPs of at least 0.5. (Temperatures towards 100 °C and higher unlock more types of and more-efficient processes, but require additional sub-component development in the collectors, in part because radiative thermal losses become non-negligible [62]. Research into this regime is on-going [63–65]). To the authors' knowledge, investigations have not yet been published into concentrating BIPVT systems designed for explicit contributions to this broad range of performance criteria: transparency, daylighting and glare control, reduced cooling loads, high-temperature cogeneration, minimized cross-section, and integration with unitized curtain wall designs and building mechanical-electrical subsystems.

1.2. Response: building integrated, transparent, concentrating PV and thermal collector

That AIF-SCs provide multiple benefits reflects the underlying utility of controlling the flow of resources between the built and natural environments. The investigation of this control paradigm motivated the development of the specific technology in this study: a Building Integrated, Transparent, Concentrating PV and Thermal collector (BITCoPT) [66–68]. BITCoPT is an actively tracked array of modules that are largely transparent to diffuse sunlight (to provide daylighting), but intercept and concentrate the direct solar component, converting it to electricity (via photovoltaics) and thermal energy, via a hydronic heat transfer circuit (Fig. 2).

The arrays of concentrating modules are integrated into a unitized curtain wall (or overhead canopy) cassette, to form the envelope system of a building (Fig. 3). The collector is designed to maximize the utility (and minimize the detriments) of envelope-incident solar energy by providing diffuse daylighting, as well as electricity and thermal energy that can used in multiple processes.

While building-integrated cogeneration is not novel, locating the collector transparently within the glazed envelope (as with BITCoPT) could encourage design of higher window-wall ratios than otherwise optimal, as its inclusion might enhance daylighting,

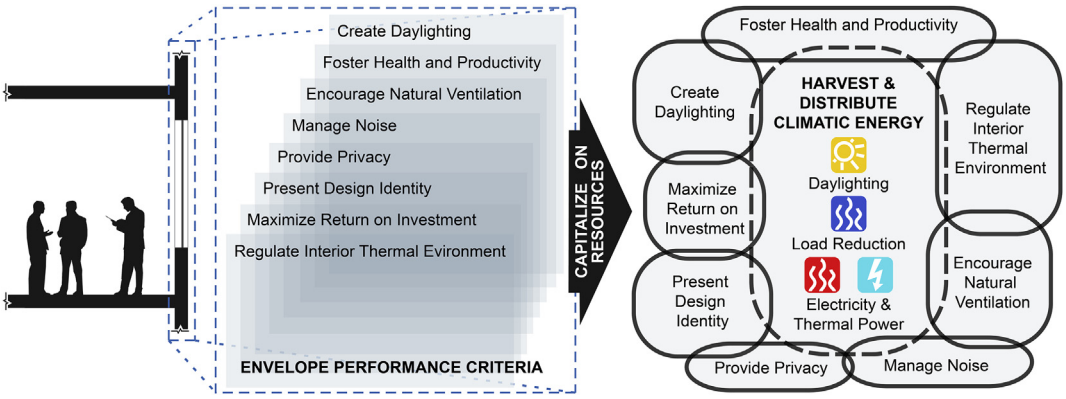

Fig. 1. Integrating energy collection and distribution to the set of responsibilities and performance criteria of building envelope.

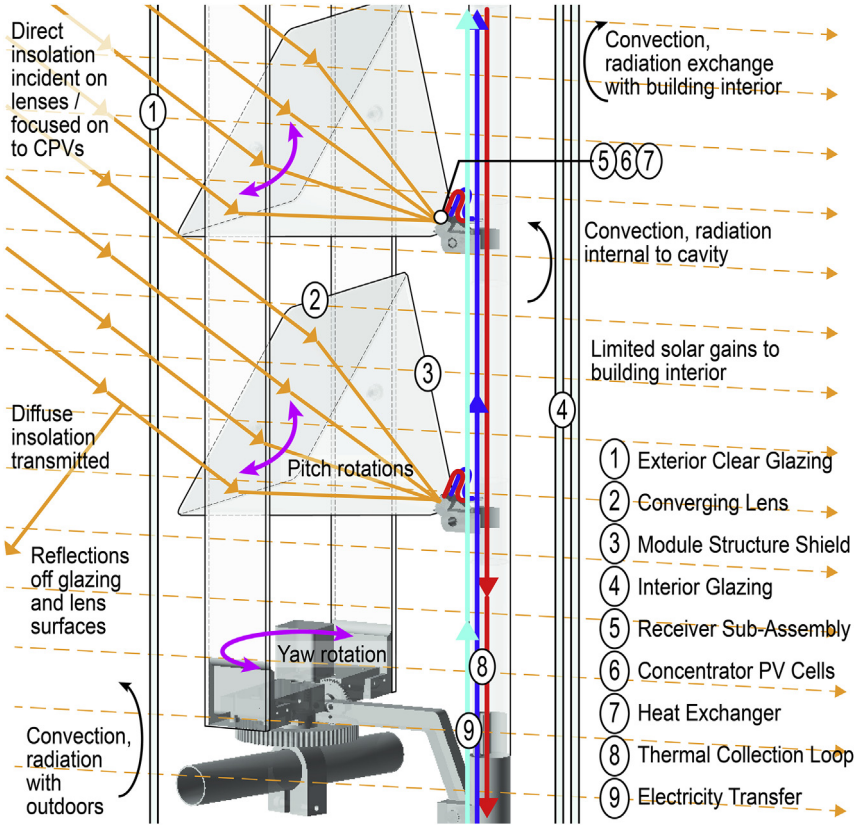

Fig. 2. Principal BITCoPT system components and energy flows showing mechanism for different treatment of direct and diffuse energy.

allow views to the exterior, and reduce cooling loads. In a shoebox-style room-scale simulation, BITCoPT demonstrated an over-50% reduction in solar gain relative to baseline solar-control glazing, with corresponding reductions in daylight glare probability [69], while in modeling an (unconditioned) train station platform environment with a solar canopy, a non-thermally active version of the system showed a 6% increase in power output over laminated BIPV, and improvements, on average, to Daylight Glare Indices across rendered viewpoints and moments (with acknowledgement that the index was conceived for indoor, side-lit environments) [70]. In experimentation, solar transmittance through the system was observed to average 0.11 under clear skies, and 0.25 under cloudy skies, indicating preferential shading-out of direct gain [71]. (A simplified prototype of the BITCoPT concept was measured that was air-cooled, and did not include active, hydronic thermal collection.)

The benefits of in-envelope concentration compound for cooling-dominated scenarios, because incident solar energy that is collected and redirected is prevented from becoming unwanted solar gain in occupied spaces and can be applied to a building's demands for service hot water and zone heating. And if, in addition to electricity, a useful fraction of the incident solar resource can be collected as thermal energy at elevated temperatures, that energy can additionally power heat engine-driven processes such as sorption chilling. These multiple effects suggest the utility of the system, considering the increasing deployment of AIF-SCs such as BIPV (Fig. 4).

The multiplicity of BITCoPT's system-level benefits, which

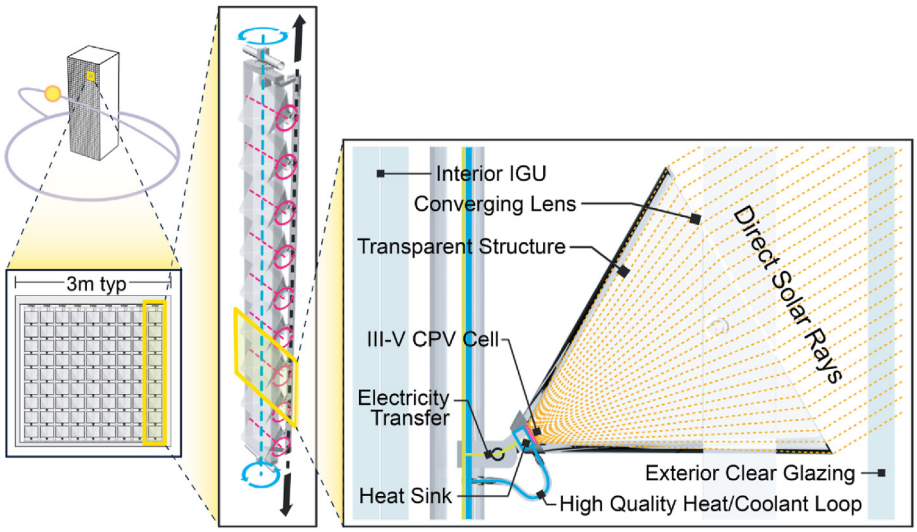

Fig. 3. Building-envelope Integrated, Transparent, Concentrating Photovoltaic and Thermal (BITCoPT) collector: inter-scalar integration with current architectural systems.

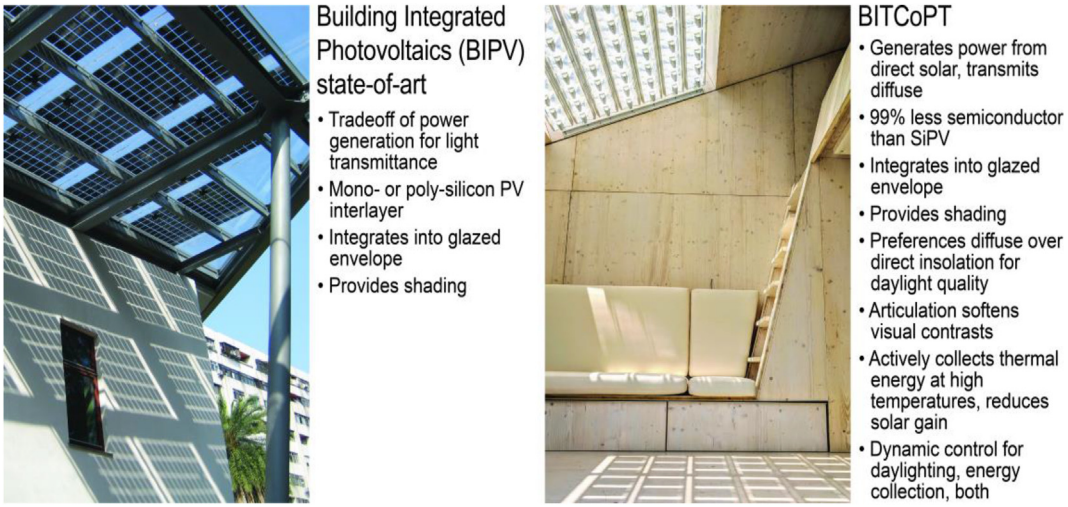

Fig. 4. Architectural integration and multifunctionality of BITCoPT relative to BIPV. Left: Taipei LEO (image: Littleha, Wikicommons.) Right: Demonstration of BITCoPT integrated in UN Environment's Ecological Living Module, at UNHQ, New York, in July 2018.

potentially make the concept impactful as a component of a building system, derive from the interaction of its contributing concepts (Fig. 5). By combining elements of multiple technologies, the system's value proposition is to collect solar power at energy and exergetic efficiencies comparable to alternative technology (such as laminated BIPV, or other mentioned actively cooled concepts), as well as gain-reduction and thermal harvesting, (as with BIST), and daylighting and glare reduction (as with diffusing or redirecting shaders), while maintaining views through to outdoors.

1.3. Research objectives: characterizing behavior of BITCoPT operational prototype and model

The objectives of this study were three-fold. Firstly, an operational prototype of the BITCoPT system was characterized in a near-full-scale installation. Secondly, a previously developed analytical model [72] was compared to data from operation of the prototype, to determine the model's capacity to represent the technology's real-world behavior. Thirdly, parameters in the model were adjusted to reflect a set of physical changes that would be undertaken in a larger-scale collector, and performance of that projected configuration was simulated.

2. Methods: Technology, model and prototype description

In this section the AIF-SC technology is described, as is the analytical model, with differences highlighted between its prototype and projected configurations. Prototype operational details and experimental setup are also described.

2.1. BITCoPT technology description

As an instance of an envelope-integrated climatic energy metabolization strategy, BITCoPT comprises an array of actively tracked, concentrating collector modules that transform insolation into electricity (via photovoltaics) and thermal energy (via a hydronic heat transfer circuit). The modules are suspended in columns (or “stacks”) in the cavity of a deep-mullion curtain wall cassette (Fig. 6).

The cassette forms the rain screen and thermal envelope of a

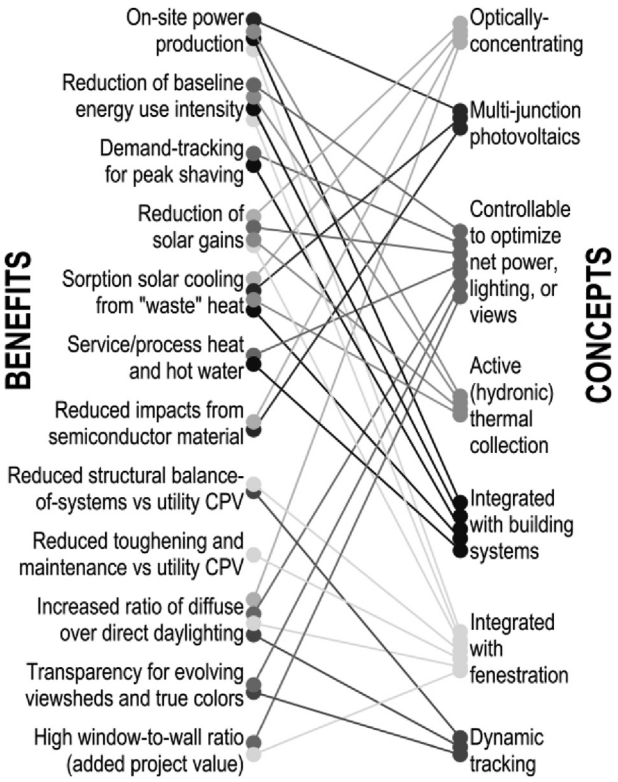

Fig. 5. Multiple system-level benefits derive from interaction of BITCoPT contributing concepts.

building, acting as a glazed exterior wall or roof. (Cassettes can also be installed in tilted orientations, to maximize solar exposure, and accommodate building designs.) The aperture of the cassette is constructed of glass or other transparent materials such as ETFE. The exterior glazing is highly transparent, to transmit solar energy to the collector modules. The inner glazing's transparency and thermal conductivity is specified according to the need of the occupied space interior to the cassette. The cassette cavity is sealed against uncontrolled infiltration from both outdoor and indoor environments, but airflow could be supplied by filtered vents, as necessary.

The BITCoPT array itself is mainly constructed from transparent components, so that building occupants enjoy views to the exterior as they would through other daylighting envelope systems (see Graphical Abstract, Fig. 6, and Fig. 7).

2.1.1. Prototype construction: concentrator module, stack and array

In the module, the fundamental unit of BITCoPT, direct irradiance is concentrated by achromatic, non-imaging lenses onto a concentrator photovoltaic cell (CPV). The CPV converts a fraction of incident insolation to electricity, while the balance is available for thermal collection via a water block heat exchanger mated to the back of the CPV (Fig. 8). A heat transfer fluid (HTF) circuit services one or more stacks of modules in series, transferring collected energy to a thermal reservoir.

The BITCoPT module includes the primary optical element (POE) and the transparent structural back-shield, which maintains alignment between the receiver, the POE, and the mechanical tracking interfaces (Fig. 8). The receiver sub-assembly includes the secondary optical element (SOE), CPV, and water block heat exchanger.

Modules are grouped into stacks that extend the height of a cassette; stacks are arrayed across the width of a cassette to fill its area. A stack consists of a pair of toughened glass fins between which the modules' "pitch" bearings are fixed, like the rungs of a ladder. The fin pairs are attached to a hanger cross piece which rotates on a "yaw" bearing located along the centerline of the stack. The bearings for each stack are suspended from a common support member that spans the width of one cassette (Fig. 7).

Modules are actively tracked to the sun's position with two degrees of freedom: the modules' rotation in the stack is the pitch axis, and the stacks' rotation in the cassette is the yaw axis. All stacks are yawed by a common linkage, while each stack has its own linkage that pitches that stack's modules (Fig. 2). Tracking is performed closed loop according to the frame reference of the machine to the sun angle, as calculated by the NOAA algorithm [73].

2.1.2. Optical design: dual-axis tracked, two-element concentrator

Direct irradiance is concentrated onto each module's CPV through a two-element Fresnel Köhler-type integrator lens

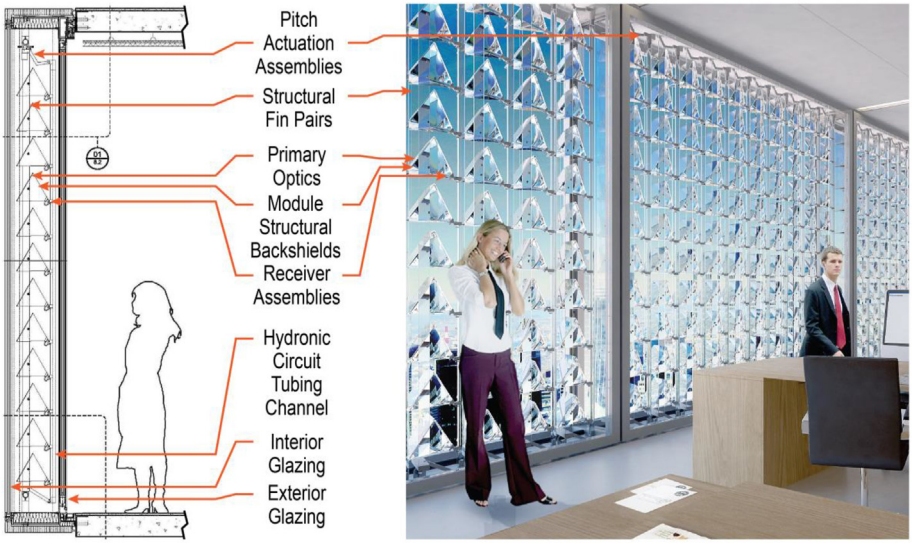

Fig. 6. A potential embodiment of BITCoPT. Left: section through a commercial building façade cassette. Right: daylighting study revealing quality of façade transparency.

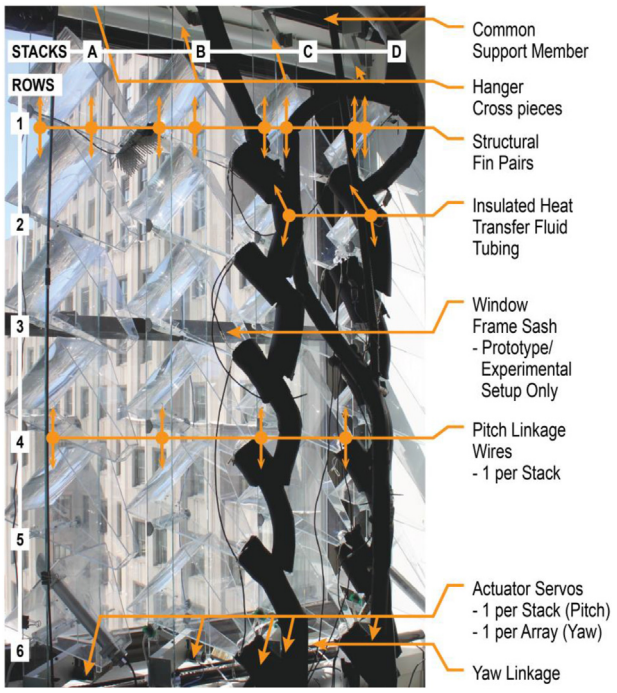

Fig. 7. BITCoPT operational prototype. Photograph taken looking out through the array and window. Arrangement of modules into stacks and array is noted.

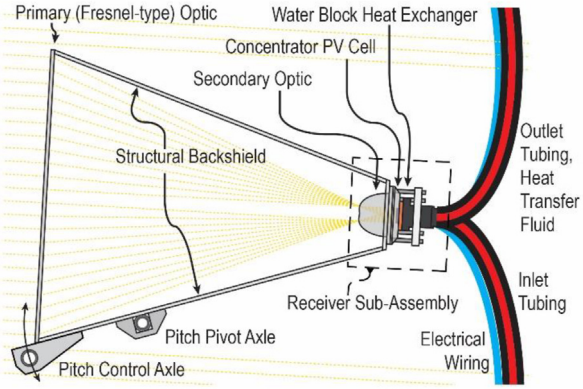

Fig. 8. BITCoPT prototype module components.

assembly. The lens design was chosen for its tolerance of off-axis illumination (the acceptable tracking error is $\leq 0.5°$) and its low sensitivity to concentration ratio. The module design is optically identical to that of the reference design [74], except for a slightly smaller POE, resulting in a concentration ratio $X_c = 615$ at f/# = 0.87. The SOE and CPV are optically coupled with an index-matched silicone elastomer. The POE is embossed PMMA, while the SOE is cast BK7 glass. Without anti-reflective (A/R) coatings on either element, the reference design's optical efficiency of 84.9%, although the observed efficiency in this experiment was lower.

2.1.3. Electrical generation: multi-junction Concentrator Photovoltaics

Direct insolation is converted to electricity by the CPV in each module. In the operational prototype, the CPV (Spectrolab C3MJ CCA100) [75] is a triple-junction cell of $A_{CPV} = 1.0\ cm^2$, mounted on an alumina back plane in parallel with a bypass diode. The CPV's nominal efficiency is $\eta_{CPV,proto} = 38.5\%$ at concentration ratio $X_{CPV} = 615$ and cell temperature $T_{CPV} = 25\ °C$. For the projected model configuration, a generalized CPV was assumed based on four-junction technology (described in Ref. [76]) with $\eta_{CPV,proj} = 42\%$. Details of modeling CPV efficiency are in Section 2.2.7.

2.1.4. Thermal energy collection: hydronic circuit

In the prototype, commercially available microprocessor coolers (Swiftech Model MCW30) were used for CPV-fluid heat exchange. The thermal resistance of these exchangers ($R_{WBHX,\ proto}$) was determined empirically. Understanding that high convection coefficients are important at low flow rates for high-concentration CPV (as noted in Ref. [77]), heat exchangers had been designed specifically for BITCoPT parameters. Although they were not employed in this prototype, the projected model configuration incorporates performance curves (provided by their manufacturer) that relate thermal resistance ($R_{WBHX,\ proj}$) to fluid flow rate (V_{HTF}). Thermal resistances are described in Section 2.2.8 and Appendix A.4.

Fluid flow in the cassette is distributed through an inlet manifold, to parallel branches of modules, which merge at an outlet manifold. In the prototype, the twelve operational modules were plumbed in series into one branch.

Thermal energy is collected in a fluid reservoir tank adjacent to BITCoPT from which fluid would be circulated to supply the various demands of a building's systems (Fig. 9). In experimentation, heat was transferred from BITCoPT to the reservoir via a crossflow heat exchanger.

2.1.5. Wall and roof integration: modular envelope cassette

Although BITCoPT is designed to operate within a ventilation-controlled cavity behind highly transparent glazing, the operational prototype was tested in a bay (an open cavity) behind a double-hung window that was fitted with insulated glazing units (IGUs) (Fig. 7). The prototype was, therefore, exposed to the conditioned interior space, rather than sealed within a cassette. The prototype is constructed with 24 modules: four stacks of six modules each. While all four stacks of modules were tracking, and optically active, only the central two stacks were instrumented for collecting cogeneration data, while the left-most and right-most stacks provided appropriate boundary conditions.

2.2. Analytical model details

The analytical model used to characterize BITCoPT is a quasi-

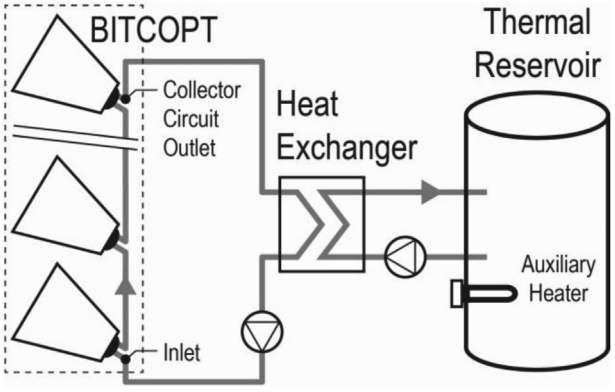

Fig. 9. Thermal collection scheme. Two hydronic circuits linked through a crossflow heat exchanger transfer thermal energy from BITCoPT to reservoir (with auxiliary heater).

steady state, lumped-capacitance representation of the system's behavior. Energy balance equations are solved for module receivers and for strings of modules at discrete time steps. The equations are described in detail in an earlier study [84], with updates explained in this section and in Appendix A.

The analytical model was used in two ways. Firstly, a set of parameters in the prototype model configuration was tuned according to data from the operational prototype, to verify the ability of the model to represent observed behavior. Secondly, a different set of parameters was modified to reflect the performance of the prototype with projected upgrades expected through further development.

2.2.1. Model inputs and outputs

Relevant variable inputs and outputs for the BITCoPT analytical model configurations are described in Table 1.

2.2.2. Solar input quantities

Three related quantities for irradiance and insolation were referenced, as described in Table 2.

The direct irradiance incident on the collector's primary optics $G_{DN,POE}$ (as measurable inside the exterior glazing of the cassette) was the reference for efficiency in the prototype model configuration. $T_{glaz,\theta}$ is the transmittance of the exterior glazing to I_{DN} (refer to Section 2.2.3). A_{POE} is the area of one module's primary lens optic (constant at $A_{POE} = 0.0626\ m^2$). F_{POE} is the unshaded fraction of the primary optic, a function of the array's pitch and yaw angles at a given time. Different subsets of modules within the BITCoPT array have different F_{POE} functions, depending on their location within the array (refer to Section 2.2.4). $G_{DN,CPV}$ is the solar energy incident on a module's CPV. This quantity applies in the receiver energy balance and as the reference for CPV conversion efficiency (refer to Section 2.2.6).

Due to uncertainties in the assembly of the prototype's modules, the optics' transmission efficiency was one of the parameters determined empirically, and then assumed constant across all modules for the prototype model configuration ($\eta_{opt,proto} = 57\%$). For the projected model configuration, the efficiency was set as reported in the literature of the reference lens design [86], with the additional assumption of an A/R coating on the SOE ($\eta_{opt,proj} = 88.6\%$). It was noted that the lower observed prototype optical efficiency could be due to poor coupling between SOE and CPV, or light leakage at the encapsulant, as has been observed in the literature [78].

2.2.3. Insolation flux through cassette glazing

BITCoPT is designed to function within a glazed cassette in a curtain wall assembly; therefore, the optical properties of the glazing were included in the analytical model. Transmittance of direct insolation ($T_{glaz,\theta}$) is attenuated by particulate soiling, bulk optical scattering, and Fresnel reflections at the boundaries between non-index-matched transparent materials (as detailed in Appendix A.1).

Table 2
Insolation and irradiance quantities.

Variable	Description, Equation
I_{DN}	Building-independent direct normal irradiance (W/m^2)
$G_{DN,POE}$	Direct normal solar power incident on collector (W): $G_{DN,POE} = I_{DN} T_{glaz,\theta} A_{POE} \sum_{i=1}^{n} F_{POE,i}$ (1)
$G_{DN,CPV}$	Solar power incident on a module CPV (W): $G_{DN,CPV} = I_{DN} T_{glaz,\theta} A_{POE} \eta_{opt} F_{POE}$ (2)

2.2.4. Module shading non-uniformity

Each module's primary optic can be partially shaded by: the cassette's frame, adjacent modules and their lenses, and the tracking structure. (Shading from external objects such as nearby buildings was not evaluated in this study.) There are nine distinct shading conditions a module might experience, depending on if the module is located along the perimeter of the array to left, right, top, or bottom, in one of the four corners, or in the central field condition. Unique look-up tables (LUTs) were generated (using geometric raytracing) for F_{POE}, the fraction of a module's primary optic that remains unshaded with respect to the array's instantaneous pitch and yaw angles. Per the generated LUTs, modules at the edges of an array are shaded, on average, 10% more than modules exhibiting the field condition, due to shadows cast by the cassette frame.

However, for the projected model configuration, because the dimensions of a typical expected use case (such as a commercial building façade or atrium canopy) would be large, the proportion of edge-condition to field-condition modules would be small, validating the assumption of a negligible edge effect. Therefore, to simplify modeling, it was assumed that all modules in the projected model configuration would exhibit the same (field) shading condition.

To model the shading conditions for the operational prototype, due to the limited size of the window bay and the crosspiece of the window's sash frame, a unique F_{POE} LUT was generated for each of the twelve operational modules (Refer to Appendix A.2 for details.).

2.2.5. Module-stack thermal circuit arrangements

In the operational prototype, the fluid circuits for the two physical stacks (of six modules each) were connected into one

Table 1
Analytical model inputs and outputs (both operational prototype and projected simulation configurations).

Model inputs	Prototype configuration	Projected configuration
BITCoPT orientation (tilt, cardinal direction)	Vertical, 40° west of south	
BITCoPT module and stack configuration	Two stacks of 6 modules, joined in series (12 total)	One stack of 10 modules
Module shading function (F_{POE})	Determined through geometric simulation	
Direct normal irradiance (I_{DN})	Measured at plane of BITCoPT array (behind glazing), modified by F_{POE}	
Heat transfer fluid inlet temperature ($T_{HTF,in}$)	Controlled with heater/thermostat	
Heat transfer fluid flow rate (V_{HTF})	Controlled, measured	Controlled
Cavity temperature (T_{cav})	Measured	
Model outputs		
Electrical generation (net: E_{gen}, efficiency: η_{Egen})	Measured and calculated	Simulated
Thermal collection (net: Q_{gen}, efficiency: η_{Qgen})	Measured and calculated	Simulated
Heat transfer fluid outlet temperature ($T_{HTF,out}$)	Measured	Simulated

series branch via an additional length (~2 m) of insulated tubing between the outlet of the first stack and the inlet of the second stack. A heat loss term was included in the prototype model configuration to represent this tubing, similar to the representation of the other tubing lengths between modules but scaled to the longer length. The projected model configuration was specified to be one physical stack, with equal tubing lengths between modules.

2.2.6. Sub-arrays for prototype measurement

Because the modules in the operational prototype experienced heterogeneous shading conditions (and therefore heterogeneous power generating characteristics), three different sub-arrays were defined (Fig. 10).

To measure electrical power generation, a homogeneously shaded, co-generating sub-array of six modules, $SA_{cogen,\ homo}$, was defined ($n_{modules,\ cogen,homo} = 6$). Because three of the modules in $SA_{cogen,\ homo}$ did not have inlet and outlet temperature sensors, to measure cogeneration from modules in the field condition, a homogeneously shaded, fully instrumented sub-array of three modules, $SA_{cogen,\ homo,FI}$, was defined ($n_{modules,\ cogen,homo,FI} = 3$). Since this sub-array was small (with higher measurement uncertainty), the full array of twelve modules SA_{hetero} was also analyzed for total output, even though not all modules were generating both electrical and thermal power ($n_{modules,\ hetero} = 12$). With heterogeneous cogeneration and shading conditions, and inlet/outlet temperature sensors, this full array of 12 modules was the basis for the calibration of model parameters.

2.2.7. CPV electrical generation efficiency

In the prototype model configuration, the CPV's electrical conversion efficiency (nominally $\eta_{CPV,nominal,\ proto} = 38.5\%$ at 25 °C) was represented by a multivariable regression of the manufacturer's data with respect to temperature and concentration ratio [87] (see Appendix A.3 for details).

For the projected model configuration, a nominal cell efficiency was determined from published data [88, [79]] to be 46.0% ± 2.2% at 22.5 °C and 508X. To experience the same concentration factor given the BITCoPT lens design, the area of the cell would be projected to increase to 118 mm^2 (10.9 mm square). The nominal projected efficiency in this study was therefore de-rated to $\eta_{CPV,nominal,\ proj} = 42.0\%$, to account for the reduction in active area, absorption effects of the larger leads required to drain current from the larger cell, and the increased shading (from the increased lead height) of the extreme angle rays from the large-aperture optics. The nominal efficiency is affected by cell temperature, which is modeled by applying linear thermal coefficients for short circuit current, open circuit voltage and fill factor.

2.2.8. Thermal collection and transport behavior

Thermal energy collected by a BITCoPT module, stack, or array was determined by

$$Q_{gen} = \dot{V}_{HTF}\rho_{HTF}c_{p,HTF}\left(T_{HTF,out} - T_{HTF,in}\right) \quad (3)$$

where V_{HTF} is the volumetric flow rate of the heat transfer fluid (m^3/s), ρ_{HTF} is the fluid density, $c_{p,HTF}$ is the fluid specific heat and T_{HTF} refers to the outlet and inlet fluid temperatures of the module, stack, or array. Thermal losses from the insulated receivers and from the insulated hydronic tubing were modeled as separate transfers across bulk resistances. This method reiterated that used in an earlier study [84], with specific updates as described in Appendix A.4.

2.2.9. Projected model configuration details

By informing the analytical model with data from operating the prototype, a projected model configuration was developed for the BITCoPT behavior that might be expected in a real-world installation. This development involved two adjustments. First, parameters and functions were modified that govern the behavior of components described earlier (glazing types, concentrating optics efficiency, water block thermal resistance, shading and stack geometry). Second, the collector's geometry was generalized to be one stack, ten modules tall. It was assumed the modules were centrally located in a BITCoPT array, as described in Section 2.2.4. The defined single stack of ten modules occupies a façade area of 0.958 m^2.

2.2.10. Energy collection (cogeneration) efficiency

The primary performance metric in this study of BITCoPT is cogeneration efficiency (η_{cogen}): the fraction of available solar energy converted to either collected thermal energy or electricity.

Efficiencies were determined relative to the solar power available on the primary optics, which was calculated from the shading look-up tables and the direct normal irradiance measured in the cassette cavity during operation. For the prototype, efficiencies were calculated for the homogenous sub-array:

$$\eta_{Egen,proto} = \frac{E_{gen}}{G_{DN,POE(n=6)}} \quad (4)$$

$$\eta_{Qgen,proto} = \frac{Q_{gen(n=3)}}{G_{DN,POE(n=3)}} \quad (5)$$

$$\eta_{cogen,proto} = \eta_{Egen,proto} + \eta_{Qgen,proto} \quad (6)$$

To project the efficiency of the BITCoPT prototype if installed in a

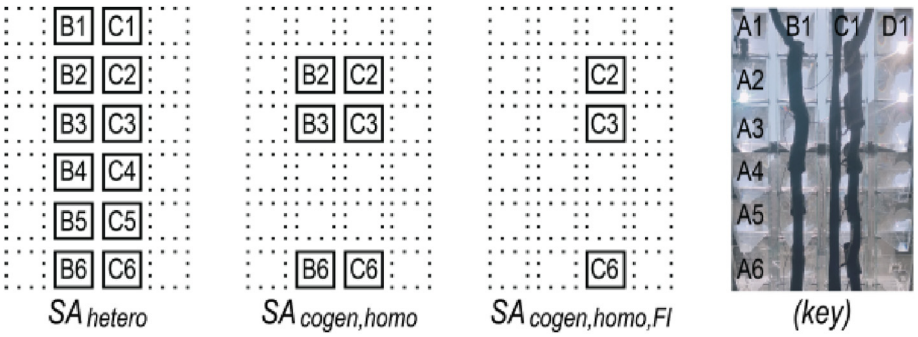

Fig. 10. Three module sub-arrays of BITCoPT operational prototype were defined: 12 modules experiencing heterogeneous shading (SA_{hetero}), 6 modules with homogeneous shading ($SA_{cogen,\ homo}$), and 3 homogeneously shaded, fully instrumented modules ($SA_{cogen,\ homo,FI}$).

real-world setting, the projected model configuration was run using the experimentally measured input conditions and building site orientation. This projected cogeneration efficiency of the prototype model configuration was calculated as:

$$\eta_{cogen,proj} = \frac{E_{gen,proj} + Q_{gen,proj}}{G_{DN,POE(n=10)}} \quad (7)$$

2.3. Operational prototype details

To characterize the behavior of the BITCoPT prototype, it was operated over a period of two months, installed in the southwest-facing window of a commercial office tower in New York City (USA), behind a double-hung window fitted with double-pane IGUs. Climatically (although the surrounding region is more temperate) due to urban heat island effect the test site in New York City is in Köppen Classification Cfa (Humid Subtropical), with an average temperature of 13 °C, extreme seasonal temperature swings, and weather-driven variations between direct-solar and diffuse-sky conditions. The site is partially shaded from buildings to the south and southwest, so the daily collection period occurred in the early afternoon, during the hours of strongest insolation in a typical day. Data from three days are presented: February 19, March 20, and March 23.

Data were collected on the flow rate and temperature of the heat transfer fluid, the air temperature in the cavity, electrical generation, direct irradiance, and the shaded fractions of the modules' primary optics. The operational prototype was outfitted with sensors as detailed in Fig. 11 and Fig. 12.

2.3.1. Measurements

Electricity generation was measured from $SA_{cogen,\ homo}$, the sub-array of six active modules that experience the same shading condition (see Fig. 10). Power was measured by sinking to an electronic load.

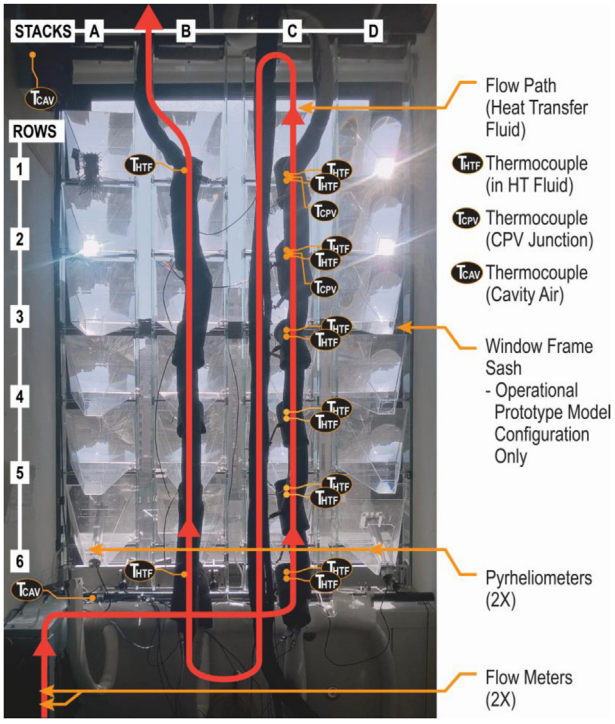

Fig. 11. BITCoPT prototype as tested, with sensor placements.

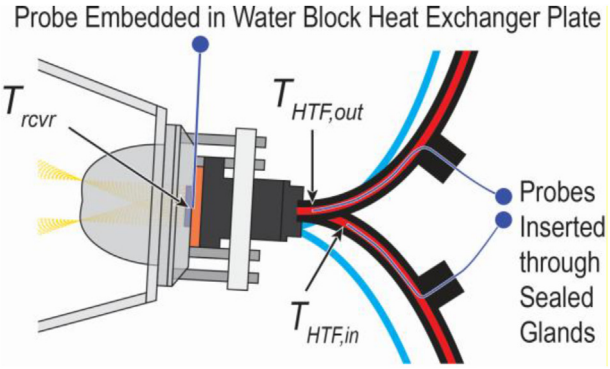

Fig. 12. Experimental setup: thermocouples installed at module receivers.

To observe thermal transfers, measurements were taken of heat transfer fluid temperature increases and flow rates both for selected individual modules and for the 12-module sub-array SA_{hetero}. Air temperatures in the bay were also measured in two locations. Data were logged through a purpose-built software interface, which also provided automated and manual trim control for the array's motion (See Appendix B.1 for details.).

3. Results: model validation; prototype and projected efficiencies

Data from the operational prototype were interpreted to fulfill three objectives: to evaluate the analytical model's predictive capacity, to determine the prototype's cogeneration efficiencies, and to project the performance of BITCoPT as it might be installed. To evaluate the model's predictive capacity, the prototype's observed behavior was compared to outputs of the prototype model simulation, relative to four measured inputs: direct normal irradiance, heat transfer fluid temperatures, fluid flow rates and cavity air temperatures. These measured inputs were then used as inputs to a simulation using the projected model configuration, so projected efficiency could be compared in a direct way to the observed behavior of the prototype.

3.1. Model validation with observed prototype data

Simulated output from the model was tuned to measured results from operation of the prototype, at the testing site in New York, NY and configured as shown in Figs. 11 and 12. Values were solved for for four parameter values in the prototype model configuration by minimizing the root mean square error (RMSE) between the simulated and observed generation and temperature signals. The parameters of interest were: optical efficiency, water block thermal resistance, heat transfer coefficients for losses from receivers to cavity air, and heat losses through tubing insulation. The compared signals were: electrical generation ($RMSE_{Egen}$ = 6.3%), thermal generation ($RMSE_{Qgen}$ = 4.3%), CPV temperatures and the fluid temperatures at tubing inlets and outlets.

Fig. 13 charts a comparison of measured to modeled values for thermal generation from all twelve modules (SA_{hetero}) and electrical power generation from the six modules in $SA_{cogen,\ homo}$, with (for reference) measured direct irradiance and inlet manifold temperature also charted.

The electricity generated by the six active modules in $SA_{cogen,\ homo}$ was relatively constant at $E_{gen} \cong 40 \pm 0.7$ W over the three collection periods. Modeled E_{gen} tracks observed E_{gen} with some

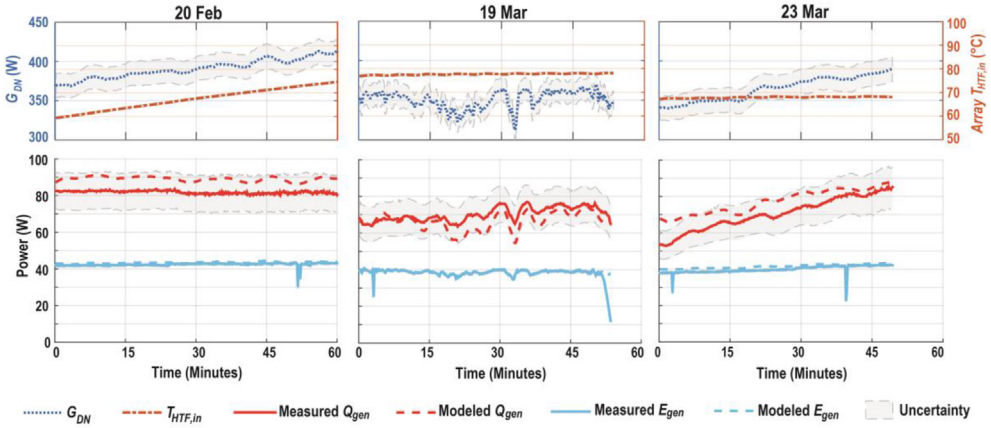

Fig. 13. Observed prototype power generation: Solar power incident on twelve modules, inlet fluid temperature, electricity generated (from $SA_{cogen,\ homo}$), thermal energy collected (from SA_{hetero}) during three reporting periods.

over-prediction during the early part of the March 23rd data. Q_{gen} in the February 20th data remained relatively constant as two conditions shifted in counteracting ways during the collection period: shadows cast from the window frame and sash decreased on the primary optics of the thermal-only modules (increasing the insolation available for collection), while inlet temperatures increased (as controlled by the auxiliary heater), decreasing the energy efficiency of collection. Because the decrease in shading was not significant on the six cogenerating modules, electrical output remained stable. In the March 19th data both E_{gen} and Q_{gen} tracked the measured irradiance, which, due to intermittent cloudiness, varied over the collection period. It should be noted that while the typical target flow rate during these periods of data acquisition is $V_{HTF} = 1.5{*}10^{-6}$ m^3/s, the flow was increased to $V_{HTF} = 3.0{*}10^{-6}$ m^3/s on March 19th to reduce the risk of fluid boiling. Although the modules tested in the prototype were neither contiguous (as they were split over two stacks) nor homogenous (being either cogenerating or thermal-only), the analytical model accounted for these heterogeneities, and the corroboration between measured and modeled outputs demonstrated that the model could reasonably be tuned to represent the behavior of the operational prototype.

3.2. Experimental cogeneration efficiency

Cogeneration efficiencies were determined from prototype operation for the fully instrumented, homogeneous sub-array $SA_{cogen,\ homo,FI}$, as charted in Fig. 14.

Over the three reporting periods, $\eta_{cogen,proto} \cong$ 35%–44% ($\eta_{Egen,proto} \cong$ 20% and $\eta_{Qgen,proto} \cong$ 15%–23%). Thermal collection ranged from 23.1% down to 17.5% as the inlet fluid temperature ranged from 58 °C up to 80 °C.

In comparing efficiency to operating temperature, the peak cogeneration energy efficiency observed was $\eta_{cogen,proto,} = 43.6\% \pm 9.1\%$, relative to module-incident direct solar energy $G_{DN,POE}$, at the lowest measured inlet temperature of 58 °C (which would be suitable for service water heating, and limited sorption chilling) as shown in Fig. 15.

At the measured temperature of 80 °C (suitable for both service water heating and sorption chilling), $\eta_{cogen,proto,} = 36.2\% \pm 7.7\%$.

3.3. Projected cogeneration efficiency

To project an optimized BITCoPT design, a simulation was run using input conditions from the February 20th experimental data. Outputs from the validated-prototype model and projected model configurations were compared (Fig. 16). The projected model configuration includes updated parameters and functions that represent nominally efficient optics; high-transparency glazing; updated CPVs; and flow-rate optimized heat exchangers (per Section 2.2).

With the projected model configuration, simulated cogeneration efficiency increased to $\eta_{cogen,proj} = 74.3\%$ (32.3% electrical and 42.0% thermal) at $T_{HTF,in} = 58$ °C, the lower bound of analyzed temperatures. At 70 °C (suitable for driving commercial adsorption chillers at nominal COP), projected efficiency was 71.2% (31.2% electrical and 40.0% thermal). At the highest analyzed temperature, 80 °C, projected efficiency was 69.4% (30.2% electrical and 39.2% thermal). Cogeneration efficiency was therefore projected to

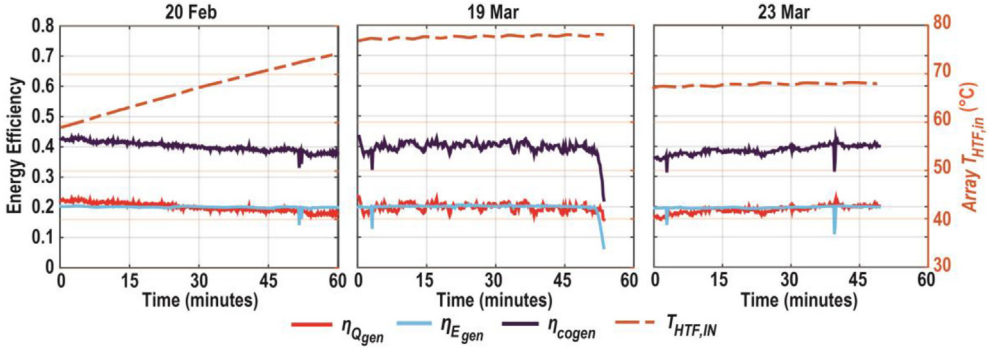

Fig. 14. Observed energy efficiencies of homogeneous sub-array $SA_{cogen,\ homo,FI}$.

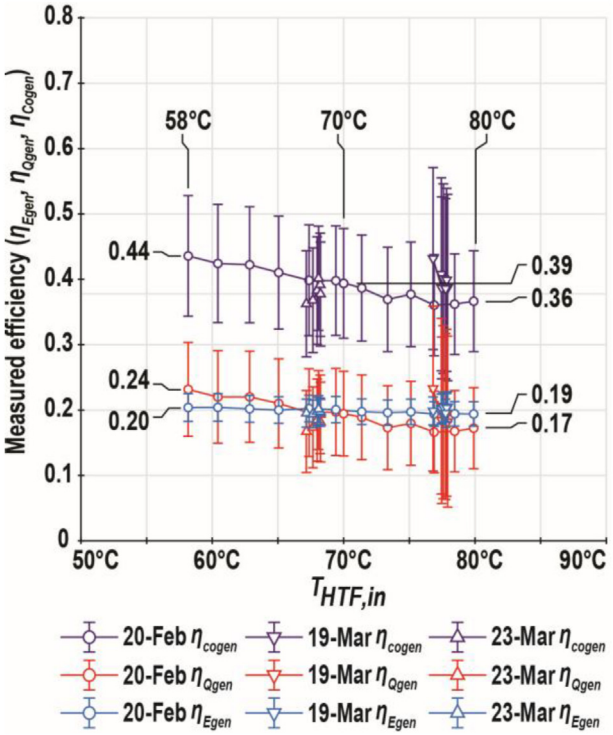

Fig. 15. Observed cogeneration efficiency η_{cogen}, for the homogenous sub-array $SA_{cogen,homo,FI}$, as a function of $T_{HTF,in}$.

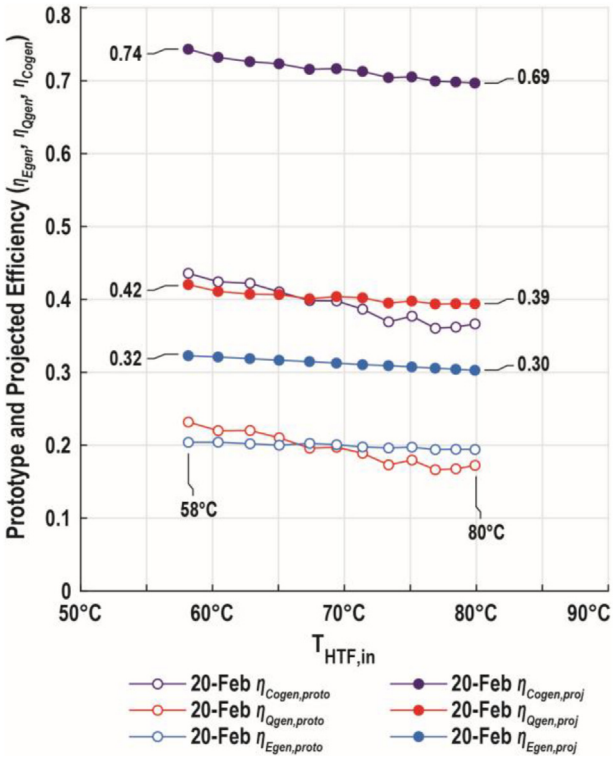

Fig. 16. Modeled prototype and projected energy efficiencies (using February 20th input conditions).

remain more stable as system temperature increased, decreasing 7% over the temperature range, relative to the observed efficiency, which decreased 18%.

4. Discussion of experimental and projected results

As seen in Section 3.3, the projected cogeneration efficiency was higher than what was experimentally observed, and maintained better as system temperatures increased. The decrease in measured efficiency with respect to inlet temperature is possibly a function of lower-than-nominal insolation reaching the CPVs, due to lack of experimental control over exterior glazing and optical efficiency in the prototype. With the increased insolation available to the CPVs ($G_{DN,CPV}$) in the projected setup, losses (which are driven by the temperature difference between the heat transfer fluid and the cavity air) are less significant. The small decrease in efficiency with respect to temperature in the projected results suggests that, if the collected thermal energy was used to drive a heat engine, there is leeway to set operating temperatures based on the engine's optimal parameters.

BITCoPT's cogeneration correlates tightly with direct irradiance (seen most clearly in Fig. 13, March 19th data), and the flat response to system temperature suggests the system could accept more intense energy without unacceptable efficiency losses. This behavior is expected from concentrating solar, and in climates with less-direct solar characteristics, the generation capacity of BITCoPT is diminished relative to non-concentrating strategies such as BIPV, reducing the energy-savings contribution to the value proposition. With multiple performance criteria influencing decisions of fenestration type, however, other criteria might “make up” for the reduced power output. For instance, in climates (such as the test location, in New York City), with volatile weather patterns, spaces with natural daylighting might experience frequent fluctuations in illuminance due to passing clouds, and BITCoPT's tempering of those variations (as noted earlier, in [83]) might have added value for commercial spaces such as the offices within which the tests were held, that typically require even lighting conditions and often reject glare and heat of direct solar gain.

As a building-integrated daylighting and shading device, BITCoPT is more complex than stand-alone solar cogeneration designs. Consequently, there are more pathways for heat loss (and less solar energy available for collection), than for stand-alone collectors. The combined efficiencies (both measured and projected) suggest, however, that this collection capacity could be useful, and warrants further investigation, especially with the added benefit of daylighting and access to exterior views, given the limited surface area that many commercial buildings have for both windows and solar collection. Given the market context of dynamic shading systems, initial projections for the system costs place it well within the upper range of current complex façade systems, while potentially providing far greater combined impacts on cooling load reductions, urban heat island impacts, and available heat, daylight, and power. Additionally, because BITCoPT is designed as a subsystem within a building's broader architectural systems, and must fulfill multiple criteria to be considered successful, useful additional analyses could include: how the cogeneration capacity affects the electrical, lighting, heating, and cooling behavior of the building; an investigation of the system's glare-reducing behavior; and qualitative characterization of the views and lighting quality provided. Broader characterization along these lines is important to understand the concept's contribution towards the overall approach and value proposition to integrated building design.

5. Summary

To develop deeper capabilities for buildings to collect and utilize solar energy, a prototype of a façade system, the Building

Integrated, Transparent, Concentrating Photovoltaic and Thermal solar collector (BITCoPT) has been characterized by fitting an analytical model to measurements from an operational prototype. BITCoPT is conceived as an example of a building envelope that dynamically mediates and buffers the energy and material flows between external and interior environments. The collector is designed to provide daylighting (by transmitting diffuse daylight) and transform direct irradiance into electricity and thermal energy, with high combined efficiency.

Results of experiments with the prototype, modeled output and extended simulations are presented and discussed. The analytical model demonstrated good ability to predict the cogeneration output of BITCoPT. Further simulations were performed with the model to explore the technology's potential performance. The prototype demonstrated a cogeneration array efficiency of up to 43.6% relative to direct irradiance that penetrates the envelope's exterior glazing layer. With adjustments to model parameters that reflect anticipated upgrades from the experimental prototype, projected cogeneration array efficiencies of 74.3% at 58 °C and 71.2% at 70 °C were simulated, suggesting the collected thermal energy would be suitable for driving heat engine processes. With the analytical model in place, future investigations can be done into the behavior of broader building systems strategies that incorporate BITCoPT.

Although the first demonstration at scale of an integrated panel into a domestic building for the UN Ecological Living Module program (see Fig. 4) showed strong appreciation of the strategy by multiple stakeholders, the potential for the acceptance and maintenance of dynamic systems in the built environment requires further investigation. Although the system ran continuously without maintenance interventions and is far less complex than it may appear, a major motivating factor for increasing acceptance would be a substantial reduction in the initial cost for environmental controls systems for heating, ventilation, cooling and electrical, due to the combined synergistic effects of simultaneously lowering building lighting and cooling loads, while providing electricity and high temperature heat for applications such as domestic hot water consumption. Additionally, the aesthetic value as well as the health and wellbeing functions of natural daylighting and thermal control need to be further quantified and qualified. In concert with providing daylighting, views to the exterior and cooling load reductions, the system addresses the physiological and psychological wellbeing of the building's occupants, by allowing far greater access to natural daylight by separating the direct from the diffuse beam. BITCoPT could generate electricity and thermal energy at a magnitude significant to commercial and other building typologies, enabling net-zero or energy-positive operation in a much wider range of circumstances than is currently considered. Equally important to the integrated energy strategy, from a material lifecycle and operations perspective, is the adaptable nature of the BITCoPT assembly, which has been designed for disassembly and reassembly, so that advances in the various components for optics, heat capture and transfer, solar conversion, etc., can be incorporated over time, allowing for an evolving integration of new technologies and methods as they emerge.

CRediT authorship contribution statement

Nick Novelli: Conceptualization, Methodology, Software, Validation, Formal analysis, Investigation, Resources, Data curation, Writing – original draft, Writing – review & editing, Visualization, Project administration. **Kenton Phillips:** Methodology, Software, Validation, Formal analysis, Investigation, Resources, Data curation, Writing – original draft, Writing – review & editing, Visualization. **Justin Shultz:** Methodology, Software, Formal analysis, Investigation, Data curation, Writing – original draft, Writing – review & editing. **Melanie M. Derby:** Validation, Writing – review & editing, Supervision. **Ryan Salvas:** Methodology, Software, Investigation, Resources, Visualization, Project administration. **Jesse Craft:** Methodology, Software, Formal analysis, Investigation, Data curation. **Peter Stark:** Conceptualization, Software, Validation, Formal analysis, Investigation, Resources, Data curation, Writing – review & editing, Visualization, Supervision, Project administration, Funding acquisition. **Michael Jensen:** Conceptualization, Methodology, Validation, Formal analysis, Resources, Writing – review & editing, Supervision, Funding acquisition. **Stephen Derby:** Conceptualization, Methodology, Funding acquisition. **Anna Dyson:** Conceptualization, Validation, Writing – original draft, Writing – review & editing, Visualization, Supervision, Funding acquisition.

Declaration of competing interest

The authors declare that they have no known competing financial interests or personal relationships that could have appeared to influence the work reported in this paper.

Acknowledgements

These findings are an expansion of work presented at the 15th Conference on Sustainable Development of Energy, Water, and Environment Systems (SDEWES) held (virtually) in Cologne, Germany, from September 1–5, 2020. The additional contributions and advisement of Kyle Brookes, Jason Vollen, Matthew Gindlesparger, Brandon Andow, Mohamed Aly and Berardo Matalucci have been instrumental in this research. The authors wish to gratefully acknowledge the funding and support from the United States Department of Energy (Grant #DE-FG36-06GO86070, 09EE0002285), the New York State Energy Research and Development Authority (NYSERDA, Grants A50417, J50367) and the New York State Office of Science, Technology and Academic Research (NYSTAR).

A. Analytical Model Details

Insolation Flux Through Cassette Glazing

Transmittance of glazing elements was modeled by

$$T_{glaz,\theta} = \left(1 - \frac{R_{sfc}}{\cos\theta_{AOI}}\right)\left[\left(1 - \frac{c_{scatt}x_{lite}}{\cos\theta_{AOI}}\right)\left(1 - \frac{2R_{Fres}}{1+R_{Fres}}\right)\right]^{n_{lites}} \tag{A.1}$$

where R_{sfc} is the attenuation from particulate soiling on the first glazing surface, θ_{AOI} is the angle of incidence between the solar vector and the element's normal vector and c_{scatt} is the coefficient of scattering in the glass material. R_{Fres} is the Fresnel reflectance from one surface (polarization independent), x_{lite} is the glazing thickness and n_{lites} is the number of glazing lites. Fresnel reflections were modeled with an approximate bidirectional reflectance distribution function [80]:

$$R_{Fres} = R_0 + (1 - R_0)(1 - \cos\theta_{AOI})^5 \quad ; \quad R_0 = \left(\frac{n_{air} - n_{glaz}}{n_{air} + n_{glaz}}\right)^2 \tag{A.2}$$

where R_0 is the reflectance at normal ($\theta_{AOI} = 0°$) while n is a material index of refraction ($n_{air} = 1.0$ and $n_{glaz} = 1.53$). Parameters for all glazing instances in both prototype and projected model configurations are given in Table A1.

Table A1
Glazing loss parameters.

Parameter	Prototype Glazing	Projected Glazing
R_{sfc}	0.030	0.0
c_{scatt} ($^{1}/_{mm}$)	0.0221	0.0075
x_{lite} (mm)	3	6
n_{lites}	2	1
T_{glaz}	0.69	0.88

Glazing properties were measured as well as analytically determined. For projected glazing instances, c_{scatt} was derived from manufacturer's data [81]. To inform the prototype model configuration, the solar transmittance of the existing double-pane window was measured to be $T_{glaz,\ proto} = 0.69$ at $\theta_{AOI} = 35°$. R_{sfc} is derived from $T_{glaz,\ proto}$. Solar transmittance $T_{glaz,\ proj}$ of the exterior glazing in the projected model configuration was modeled as a single thickness of low-iron glass ($T_{glaz,\ proj} = 0.88$).

Module Shading Non-Uniformity

Due to the geometry of the double-hung window bay into which the operational prototype was installed, a unique F_{poe} LUT (relative to array yaw and pitch) was generated for each active module, using geometric ray tracing. An instance of the ray tracing is shown in Fig. A.1.

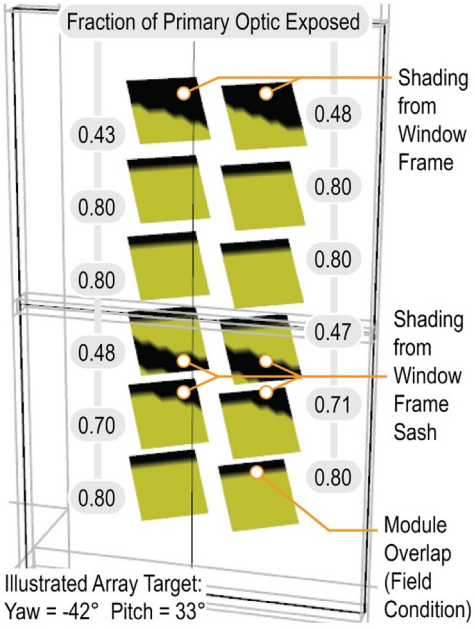

Fig. A.1. Simulation of angle-dependent shading conditions (F_{POE}) used to generate unique LUTs for each module in prototype model configuration.

CPV Electrical Generation Efficiency

CPV conversion efficiency for the prototype model configuration was modeled as follows:

$$\eta_{CPV} = \frac{E_{gen}}{G_{DN,CPV}} \tag{A.3}$$

$$\eta_{CPV,proto} = 36.4 + 5.0 \times 10^{-4}(52.5 - (T_{CPV} - 273.15)) + \left(1.997 \times 10^{-6}\right)(X_{CPV} - 627.5) \tag{A.4}$$

Because the coefficient for the X_{CPV} term is negligible relative to the coefficient for the T_{CPV} term, the concentration ratio was assumed constant and equal to the optical ratio X_{opt}: $X_{CPV} = 615$.

Nominal CPV efficiency in the projected model configuration is affected by cell temperature, which is modeled by applying linear thermal coefficients for short circuit current, open circuit voltage and fill factor:

$$\eta_{CPV,proj} = \eta_{nominal,\ c4J} * [1 - (1 - k_{sc})(1 - k_{oc})(1 - k_{FF}) \times (T_{CPV} - T_{CPV,nominal})] \tag{A.5}$$

where the thermal coefficients are: $k_{SC} = 0.1\%/K$ for the short circuit current; $k_{OC} = -0.14\%/K$ for the open circuit voltage; and $k_{FF} = -0.18\%/K$ for the fill factor, per the literature [82]. The variation of η_{CPV} with incident flux density was neglected, as in the observed data most energy was produced during periods with strong irradiance, where flux density did not vary greatly.

Thermal Collection and Transport Behavior

Specific heat and density were assumed constant at $c_{p,HTF} = 4.190\ ^{kJ}/_{kg\text{-}K}$ and $\rho_{HTF} = 974.9\ ^{kg}/_{m}^{3}$, corresponding to an average fluid temperature of 75 °C.

The resistance to heat flow across the water block heat exchanger (R_{WBHX}) was modeled by different methods from the prototype to the projected model configurations. For the prototype model configuration, with Q_{gen} known, the temperature difference across the water block was measured, comparing the temperature measured (via embedded probe) at the CPV-water block mating surface (T_{CPV}) to the log-mean temperature of the fluid in the heat exchanger ($T_{HTF,LMT}$):

$$R_{WBHX,proto} = \frac{T_{CPV} - T_{HTF,LMT}}{\dot{V}_{HTF}\rho_{HTF}c_{p,HTF}(T_{HTF,out} - T_{HTF,in})} \tag{A.6}$$

The water block thermal resistance was determined to be $R_{WBHX,\ proto} = 0.90$ K/W and 0.70 K/W at $V_{HTF} = 1.5{*}10^{-6}$ m^3/s and $3{*}10^{-6}$ m^3/s, respectively. For the projected model configuration, the custom-spec heat exchanger was modeled with a regression of the manufacturer's data describing R_{WBHX} relative to mass flow:

$$R_{WBHX,proj} = 0.2487\left(\left(10^{6}\right)\dot{V}_{HTF}\right)^{-0.773} \tag{A.7}$$

Consideration of Parasitic and Radiation Terms

Two parasitic electrical losses are inherent in BITCoPT: electrical power draw from the tracking actuators and HTF pumps. These would represent a small fraction of the generation output of a full-scale installation. Because the objectives of this analysis were to measure cogeneration and to calibrate the model, tracking power and pumping losses were not included, because they are not represented in the scope of the modeled system.

Re-radiation energy transfers in the system become substantial as surface temperatures increase, particularly past 100 °C, as noted in the literature [74]. Because the operating range of the current BITCoPT design is below that threshold, radiation is not modeled independently from the other heat loss terms. Collector designs with higher concentration ratios might benefit from more detailed modeling of the multiple thermal transfer mechanisms.

B. Measurements, Control, Data Acquisition and Reduction

Methods of Measurements and Control

Electrical power generated by the serial string of modules was measured by sinking power to an electronic load (BK Precision 8500). The string's maximum power point was dynamically tracked to within ±0.1 V through manual adjustments. The measured modules were connected in series. 12AWG or larger copper wire was used to minimize voltage drop in the module circuit. Direct irradiance was measured with a pair of pyrheliometers (Hukseflux DR01), which were 3rd-party calibrated prior to data acquisition. Beyond the usefulness of redundancy, dual instruments were utilized so that, at any given time in the operation of the prototype, one sensor was exposed to the sun, and not shaded by the frame of the window aperture.

To measure the rise in temperature from individual modules, fluid temperatures were measured with thermocouple probes at the water blocks' inlets and outlets (Fig. 11). These thermocouples were installed on the six modules in the third stack and the first and sixth modules of the second stack (denoted T_{HTF} in Fig. 11). The temperature rise from the branch of modules was taken to be the difference between the temperature at the inlet of the first module in the branch and at the outlet of the last module. The tubing that connected the heat exchangers was insulated with low density neoprene foam ($k = 0.0372$ W/m-K at 32 °C) to a minimum thickness of 18 mm.

Heat transfer fluid flow rates were measured with float-type volumetric flow meters (Porter F150-B125-60). To mitigate measurement error, flow rates and floats were picked so that, for typical rates ($V_{HTF} = 1.5{*}10^{-6}$ m^3/s), readings were at half-height or higher on their scales and the temperature rise across the branch was large relative to the measurement error stack-up. In the projected model configuration, the thermal resistance across the modeled heat exchanger increases with flow rate. In the prototype, however, varying flow rates had little effect on thermal collection, likely due to the high flow capacity of the commercial water block heat exchangers used, which would result in similar flow regimes for all tested flow rates.

Fluid temperatures were measured with thermocouple probes inserted into the flow through packing glands (Fig. 12). The thermocouples were T-type (from Omega Engineering), ungrounded and in 1 mm diameter stainless steel probe sheaths. At selected modules additional temperatures were taken at the mating surface between the water block heat exchanger and the CPV (Figs. 11 and 12). The ambient air temperature in the window bay cavity ($T_{cav,proto}$) was measured with bare, ungrounded K-type thermocouples (from Omega) in free air, in two locations: in the upper and lower corners of the bay, and at the foot of the bay, at the outlet of a fan coil unit that supplies tempered air (a component of the laboratory's HVAC systems).

Because of the relatively small temperature differences across each receiver water block, the thermocouples were calibrated individually prior to experimentation by noting their readings in both a well-stirred ice bath and a water bath at a consistent rolling boil. The averages (means) of each sensor's sample set of readings were then used to offset the lower and upper end of the sensors' voltage-temperature response curves.

The thermal collection circuit is documented in Fig. 9. In the operational prototype, flow in the collector circuit was driven by a positive-displacement pump (Pentair pump GCBN23V) at a constant speed. Pressure (and therefore flow rate) was modulated by means of a bypass branch with a needle valve control. Flow passed through a liquid/liquid plate heat exchanger before returning to the pump, and a separate fluid circuit joined the second side of the heat exchanger (in counter-flow) to a reservoir tank, containing 10 kg of water (or 42 kJ/K heat capacity). The tank was fitted with a thermostatically controlled 1 kW heating element, which maintained the collector circuit inlet temperature to within ±0.5 °C of the chosen set point. The reservoir circuit was pressurized with a low-head, high-flow circulator (Bell and Gossett NBF-220, 0.12hp). Both circuits were fitted with expansion, bypass, and fill mechanisms.

Data acquisition was performed on a PC through an interface developed in the LabVIEW environment. Logged measurements are noted in Table 1. All measurements were taken and logged automatically, except for flow rates, which were periodically read at the flow meters and logged through the interface.

The prototype was controlled by software developed in the LabVIEW environment. The software determined a yaw target for the array and pitch targets for each stack, in open-loop control, based on: the solar vector, the orientation of the array in space, and alignment trims for each axis. The solar vector was calculated according to NOAA's solar position algorithm [85]. Axis targets were sent serially to an embedded motion controller which referenced rotational encoders mounted on each yaw and pitch axis (five total). It was observed that rotational jogs of less than 0.1° could be repeated reliably on all axes, well within the ±0.5° optical alignment tolerance (Section 2.1.2).

Steady-State Definition

Because the changes in observed system state and inputs were slow relative to the time constants of the systems thermal masses, steady-state operation was assumed in the system models. Analyzed datasets were therefore restricted to time periods that approximated steady-state operation. The system was observed to be in a steady state when changes in the temperature increase across it were sufficiently gradual such that

$$\frac{d}{dt}\left(T_{HTF,out} - T_{HTF,in}\right) \leq 0.026\left(\frac{1}{s}\right) T_{HTF,in} \tag{B.1}$$

The principal cause of non-steady state operation was observed to be fluctuations in input solar power, which drove system temperatures (and power output) at a lag due to low heat transfer fluid flow rates and the heat capacities of receiver components. However gradual shifts in inputs were not observed to disrupt steady-state behavior, where

$$\frac{d}{dt}G_{DN,POE} \leq 0.10\left(\frac{1}{s}\right) G_{DN,POE} \tag{B.2}$$

Data for characterization was chosen from periods of time when these two conditions were met.

Uncertainty Characterization

Uncertainty in thermal collection (Δ_{Qgen}) stems from temperature and flow rate measurements as well as the correlations used for specific heat values and density.

$$\Delta_{Q_{gen}} = \left[\left(\rho_{HTF} c_{p,HTF} (T_{out} - T_{in})\right)^2 \Delta_{\dot{V}}{}^2 + \left(\dot{V}_{HTF} c_{p,HTF} (T_{out} - T_{in})\right)^2 \Delta_{\rho}^2 + \left(\dot{V}_{HTF} \rho_{HTF} (T_{out} - T_{in})\right)^2 \Delta_{c_{p,HTF}}^2 + \left(- \dot{V}_{HTF} \rho_{HTF} c_{p,HTF}\right)^2 \Delta_{T_{out}}^2 + \left(\dot{V}_{HTF} \rho_{HTF} c_{p,HTF}\right)^2 \Delta_{T_{in}}^2 \right]^{\frac{1}{2}} \quad \text{(B.3)}$$

Because Δ_{Qgen} was high relative to a module's thermal power output, this output was characterized for the entire branch of modules.

Uncertainty in electrical collection (Δ_{Egen}) stemmed from the measurement of generated power. Relative to Δ_{Qgen}, Δ_{Egen} was minor at 0.73 W.

$$\Delta_{E_{gen}} = \left[I^2 \Delta_V{}^2 + V^2 \Delta_I{}^2 \right]^{\frac{1}{2}} \quad \text{(B.4)}$$

Uncertainties of experimental results are characterized using propagation of uncertainty analysis, which assume no covariance between measurements. Table B1 lists the uncertainties for the measured values in the experiment, where FS indicates full-scale reading, with values shown in parentheses.

Table B1
List of Uncertainties.

Parameter	Uncertainty (Absolute or Relative)
$\dot{V}_{HTF}$	±5% FS (3.5 *10^{-6} m^3/s)
c_p	±1% 4190 J/kg-K
ρ_{HTF}	±1% 974.9 kg/m^3
T_{HTF}	±0.5 °C (T-type), 1.1 °C (K-type)
V_{gen}	±0.05% + 0.025% FS (120 V)
I_{gen}	±0.2% + 0.15% FS (30 A)
I_{DN}	±1.2%
F_{POE}	±3%

References

[1] B.A. Statham, World Energy Council, Deciding the Future: Energy Policy Scenarios to 2050, World Energy Council, London, 2013.

[2] S. Bringezu, A. Ramaswami, H. Schandl, M. O'Brien, R. Pelton, J. Acquatella, E.T. Ayuk, A.S.F. Chiu, R. Flanegin, J. Fry, S. Giljum, S. Hashimoto, S. Hellweg, K. Hosking, Y. Hu, M. Lenzen, M. Lieber, S. Lutter, M. Alessio, et al., *Assessing Global Resource Use: A Systems Approach to Resource Efficiency and Pollution Reduction* (IRP UNEP 162; IRP, UNEP, 2017, p. 104. https://www.resourcepanel.org/reports/assessing-global-resource-use.

[3] UN, Transforming our world: the 2030 agenda for sustainable development: sustainable development knowledge platform, Retrieved July 19, 2020, from, https://sustainabledevelopment.un.org/post2015/transformingourworld, 2015.

[4] A. Dyson, T. Ngai, J. Vollen, Characterizing the problem: bioenergetic information modeling, in: BIM in Academia, Yale School of Architecture, 2011.

[5] R.R. Hernandez, M.K. Hoffacker, C.B. Field, Land-use efficiency of big solar, Environ. Sci. Technol. 48 (2) (2014) 1315–1323.

[6] M.G. Figueiro, B. Steverson, J. Heerwagen, K. Kampschroer, C.M. Hunter, K. Gonzales, B. Plitnick, M.S. Rea, The impact of daytime light exposures on sleep and mood in office workers, Sleep Health 3 (3) (2017) 204–215, https://doi.org/10.1016/j.sleh.2017.03.005.

[7] A.D. Galasiu, J.A. Veitch, Occupant preferences and satisfaction with the luminous environment and control systems in daylit offices: a literature review, Energy Build. 38 (7) (2006) 728–742, https://doi.org/10.1016/j.enbuild.2006.03.001.

[8] I. Turan, A. Chegut, D. Fink, C. Reinhart, The value of daylight in office spaces, Build. Environ. 168 (2020), 106503, https://doi.org/10.1016/j.buildenv.2019.106503.

[9] I.C. Mason, M. Boubekri, M.G. Figueiro, B.P. Hasler, S. Hattar, S.M. Hill, R.J. Nelson, K.M. Sharkey, K.P. Wright, W.A. Boyd, M.K. Brown, A.D. Laposky, M.J. Twery, P.C. Zee, Circadian health and light: a report on the national heart, lung, and blood institute's workshop, J. Biol. Rhythm. 33 (5) (2018) 451–457, https://doi.org/10.1177/0748730418789506.

[10] A. Nabil, J. Mardaljevic, Useful daylight illuminances: a replacement for daylight factors, Energy Build. 38 (7) (2006) 905–913, https://doi.org/10.1016/j.enbuild.2006.03.013.

[11] P.J. Littlefair, The luminous efficacy of daylight: a review, Light. Res. Technol. 17 (4) (1985) 162–182, https://doi.org/10.1177/14771535850170040401.

[12] Vasilis M. Fthenakis, Hyung Chul Kim, Life cycle assessment of high-concentration photovoltaic systems: life cycle assessment of PV systems, Prog. Photovoltaics Res. Appl. 21 (2013) 379–388, https://doi.org/10.1002/pip.1186.

[13] K. Menoufi, D. Chemisana, J.I. Rosell, Life cycle assessment of a building integrated concentrated photovoltaic scheme, Appl. Energy 111 (2013) 505–514, https://doi.org/10.1016/j.apenergy.2013.05.037.

[14] M. Raugei, N. Keena, N. Novelli, M.A. Etman, A. Dyson, Life cycle assessment of an ecological living module equipped with conventional rooftop or integrated concentrating photovoltaics, J. Ind. Ecol. (2021), https://doi.org/10.1111/jiec.13129.

[15] P. Heiselberg (Ed.), *Integrating Environmentally Responsive Elements in Buildings* (Annex No. 44), IEA/ECBCS, 2012. http://www.ecbcs.org/docs/ECBCS_Annex_44_PSR.pdf.

[16] S. Attia, S. Bilir, T. Safy, C. Struck, R. Loonen, F. Goia, Current trends and future challenges in the performance assessment of adaptive façade systems, Energy Build. 179 (2018) 165–182, https://doi.org/10.1016/j.enbuild.2018.09.017.

[17] A.V. Thomas, B.C. Andow, S. Suresh, O. Eksik, J. Yin, A.H. Dyson, N. Koratkar, Controlled crumpling of graphene oxide films for tunable optical transmittance, Adv. Mater. 27 (21) (2015) 3256–3265, https://doi.org/10.1002/adma.201405821.

[18] Y. Zhai, Y. Ma, S.N. David, D. Zhao, R. Lou, G. Tan, R. Yang, X. Yin, Scalable-manufactured randomized glass-polymer hybrid metamaterial for daytime radiative cooling, Science 355 (6329) (2017) 1062–1066, https://doi.org/10.1126/science.aai7899.

[19] E.A. Goldstein, A.P. Raman, S. Fan, Sub-ambient non-evaporative fluid cooling with the sky, Nat. Energy 2 (9) (2017) 1–7, https://doi.org/10.1038/nenergy.2017.143.

[20] S.G. Colaco, C.P. Kurian, V.I. George, A.M. Colaco, Prospective techniques of effective daylight harvesting in commercial buildings by employing window glazing, dynamic shading devices and dimming control—a literature review, Build. Simulat. 1 (4) (2008) 279–289, https://doi.org/10.1007/s12273-008-8126-8.

[21] A. Tzempelikos, The impact of Venetian blind geometry and tilt angle on view, direct light transmission and interior illuminance, Sol. Energy 82 (12) (2008) 1172–1191, https://doi.org/10.1016/j.solener.2008.05.014.

[22] I. Konstantzos, A. Tzempelikos, Y.-C. Chan, Experimental and simulation analysis of daylight glare probability in offices with dynamic window shades, Build. Environ. 87 (2015) 244–254, https://doi.org/10.1016/j.buildenv.2015.02.007.

[23] M. Konstantoglou, A. Tsangrassoulis, Dynamic operation of daylighting and shading systems: a literature review, Renew. Sustain. Energy Rev. 60 (2016) 268–283, https://doi.org/10.1016/j.rser.2015.12.246.

[24] H. Gholami, H.N. Røstvik, D. Müller-Eie, Holistic economic analysis of building integrated photovoltaics (BIPV) system: case studies evaluation, Energy Build. 203 (2019), 109461, https://doi.org/10.1016/j.enbuild.2019.109461.

[25] G. Quesada, D. Rousse, Y. Dutil, M. Badache, S. Hallé, A comprehensive review of solar facades. Transparent and translucent solar facades, Renew. Sustain. Energy Rev. 16 (5) (2012) 2643–2651.

[26] C. Lamnatou, J.D. Mondol, D. Chemisana, C. Maurer, Modelling and simulation of Building-Integrated solar thermal systems: behaviour of the system, Renew. Sustain. Energy Rev. 45 (2015) 36–51.

[27] G. Kiss, J. Kinkead, M. Raman, Building-Integrated Photovoltaics: A Case Study (No. NREL/TP–472-7574), National Renewable Energy Lab., Golden, CO (United States), 1995.

[28] J.A. Clarke, J.W. Hand, C.M. Johnstone, N. Kelly, P.A. Strachan, Photovoltaic-integrated building facades, Renew. Energy 8 (1–4) (1996) 475–479.

[29] I. Zanetti, P. Bonomo, F. Frontini, E. Saretta, M. van den Donker, G. Verberne, K. Sinapis, W. Folkerts, Building Integrated Photovoltaics: Product Overview for Solar Building Skins Status Report, SUPSI-University of Applied Sciences and Arts of Southern Switzerland, 2017.

[30] K. Peippo, P.D. Lund, E. Vartiainen, Multivariate optimization of design trade-

offs for solar low energy buildings, Energy Build. 29 (2) (1999) 189–205.
[31] R.C.G.M. Loonen, M. Trčka, D. Cóstola, J.L.M. Hensen, Climate adaptive building shells: state-of-the-art and future challenges, Renew. Sustain. Energy Rev. 25 (2013) 483–493.
[32] P.K. Ng, N. Mithraratne, H.W. Kua, Energy analysis of semi-transparent BIPV in Singapore buildings, Energy Build. 66 (2013) 274–281.
[33] A. Karthick, K. Kalidasa Murugavel, L. Kalaivani, Performance analysis of semitransparent photovoltaic module for skylights, Energy 162 (2018) 798–812, https://doi.org/10.1016/j.energy.2018.08.043.
[34] L. Olivieri, E. Caamaño-Martin, F. Olivieri, J. Neila, Integral energy performance characterization of semi-transparent photovoltaic elements for building integration under real operation conditions, Energy Build. 68 (Part A) (2014) 280–291.
[35] Y. Cheng, M. Gao, J. Dong, J. Jia, X. Zhao, G. Li, Investigation on the daylight and overall energy performance of semi-transparent photovoltaic facades in cold climatic regions of China, Appl. Energy 232 (2018) 517–526, https://doi.org/10.1016/j.apenergy.2018.10.006.
[36] M.D. Bazilian, F. Leenders, B.G. Van der Ree, D. Prasad, Photovoltaic cogeneration in the built environment, Sol. Energy 71 (1) (2001) 57–69.
[37] C. Good, J. Chen, Y. Dai, A.G. Hestnes, Hybrid photovoltaic-thermal systems in buildings – a review, Energy Procedia 70 (2015) 683–690, https://doi.org/10.1016/j.egypro.2015.02.176.
[38] T. Yang, A.K. Athienitis, A review of research and developments of building-integrated photovoltaic/thermal (BIPV/T) systems, Renew. Sustain. Energy Rev. 66 (Supplement C) (2016) 886–912, https://doi.org/10.1016/j.rser.2016.07.011.
[39] A.K. Athienitis, G. Barone, A. Buonomano, A. Palombo, Assessing active and passive effects of façade building integrated photovoltaics/thermal systems: dynamic modelling and simulation, Appl. Energy 209 (2018) 355–382, https://doi.org/10.1016/j.apenergy.2017.09.039.
[40] M.J.M. Pathak, P.G. Sanders, J.M. Pearce, Optimizing limited solar roof access by exergy analysis of solar thermal, photovoltaic and hybrid photovoltaic thermal systems, Appl. Energy 120 (2014) 115–124.
[41] M. Herrando, A.M. Pantaleo, K. Wang, C.N. Markides, Solar combined cooling, heating and power systems based on hybrid PVT, PV or solar-thermal collectors for building applications, Renew. Energy 143 (2019) 637–647, https://doi.org/10.1016/j.renene.2019.05.004.
[42] X. Zhang, J. Shen, P. Xu, X. Zhao, Y. Xu, Socio-economic performance of a novel solar photovoltaic/loop-heat-pipe heat pump water heating system in three different climatic regions, Appl. Energy 135 (2014) 20–34.
[43] S. Saadon, L. Gaillard, C. Menezo, S. Giroux-Julien, Exergy, exergoeconomic and enviroeconomic analysis of a building integrated semi-transparent photovoltaic/thermal (BISTPV/T) by natural ventilation, Renew. Energy 150 (2020) 981–989, https://doi.org/10.1016/j.renene.2019.11.122.
[44] N. Gupta, G.N. Tiwari, Parametric study to understand the effect of various passive cooling concepts on building integrated semitransparent photovoltaic thermal system, Sol. Energy 180 (2019) 391–400, https://doi.org/10.1016/j.solener.2018.12.079.
[45] K. Vats, G.N. Tiwari, Energy and exergy analysis of a building integrated semitransparent photovoltaic thermal (BISPVT) system, Appl. Energy 96 (2012) 409–416, 0.
[46] A. Buonomano, F. Calise, A. Palombo, M. Vicidomini, Adsorption chiller operation by recovering low-temperature heat from building integrated photovoltaic thermal collectors: modelling and simulation, Energy Convers. Manag. 149 (2017) 1019–1036, https://doi.org/10.1016/j.enconman.2017.05.005.
[47] G. Li, Q. Xuan, M.W. Akram, Y. Golizadeh Akhlaghi, H. Liu, S. Shittu, Building integrated solar concentrating systems: a review, Appl. Energy 260 (2020), 114288, https://doi.org/10.1016/j.apenergy.2019.114288.
[48] D. Chemisana, J. López-Villada, A. Coronas, J.I. Rosell, C. Lodi, Building integration of concentrating systems for solar cooling applications, Appl. Therm. Eng. 50 (2) (2013) 1472–1479.
[49] D. Chemisana, J.I. Rosell, A. Riverola, C. Lamnatou, Experimental performance of a Fresnel-transmission PVT concentrator for building-façade integration, Renew. Energy 85 (2016) 564–572, https://doi.org/10.1016/j.renene.2015.07.009.
[50] Y. Wu, K. Connelly, Y. Liu, X. Gu, Y. Gao, G.Z. Chen, Smart solar concentrators for building integrated photovoltaic façades, Sol. Energy 133 (2016) 111–118, https://doi.org/10.1016/j.solener.2016.03.046.
[51] Y. Tripanagnostopoulos, C. Siabekou, J.K. Tonui, The Fresnel lens concept for solar control of buildings, Sol. Energy 81 (5) (2007) 661–675.
[52] M. Sabry, P.C. Eames, H. Singh, Y. Wu, Smart windows: thermal modelling and evaluation, Sol. Energy 103 (Supplement C) (2014) 200–209, https://doi.org/10.1016/j.solener.2014.02.016.
[53] R. Gorthala, Tri-sol (Building-Integrated, three-in-one solar) technology development, in: ASME 2015 9th International Conference on Energy Sustainability, 2015, https://doi.org/10.1115/ES2015-49437.
[54] H. Baig, N. Sellami, T.K. Mallick, Performance modeling and testing of a building integrated concentrating photovoltaic (BICPV) system, Sol. Energy Mater. Sol. Cell. 134 (Supplement C) (2015) 29–44, https://doi.org/10.1016/j.solmat.2014.11.019.
[55] L.A.A. Bunthof, F.P.M. Kreuwel, A. Kaldenhoven, S. Kin, W.H.M. Corbeek, G.J. Bauhuis, E. Vlieg, J.J. Schermer, Impact of shading on a flat CPV system for façade integration, Sol. Energy 140 (2016) 162–170, https://doi.org/10.1016/j.solener.2016.11.001.
[56] L. Zhu, Z. Shao, Y. Sun, V. Soebarto, F. Gao, G. Zillante, J. Zuo, Indoor daylight distribution in a room with integrated dynamic solar concentrating facade, Energy Build. 158 (Supplement C) (2018) 1–13, https://doi.org/10.1016/j.enbuild.2017.10.008.
[57] G. Li, Q. Xuan, X. Zhao, G. Pei, J. Ji, Y. Su, A novel concentrating photovoltaic/daylighting control system: optical simulation and preliminary experimental analysis, Appl. Energy 228 (2018) 1362–1372, https://doi.org/10.1016/j.apenergy.2018.07.024.
[58] W. Lu, Y. Wu, P. Eames, Design and development of a building façade integrated asymmetric compound parabolic photovoltaic concentrator (BFI-ACP-PV), Appl. Energy 220 (2018) 325–336, https://doi.org/10.1016/j.apenergy.2018.03.071.
[59] T. Ulavi, T. Hebrink, J.H. Davidson, Analysis of a hybrid solar window for building integration, Sol. Energy 105 (2014) 290–302.
[60] T.P. Otanicar, S. Theisen, T. Norman, H. Tyagi, R.A. Taylor, Envisioning advanced solar electricity generation: parametric studies of CPV/T systems with spectral filtering and high temperature PV, Appl. Energy 140 (2015) 224–233.
[61] A. Buonomano, F. Calise, M. Dentice d'Accadia, L. Vanoli, A novel solar trigeneration system based on concentrating photovoltaic/thermal collectors. Part 1: design and simulation model, Energy 61 (2013) 59–71, https://doi.org/10.1016/j.energy.2013.02.009.
[62] Y.V. Vorobiev, J. González-Hernández, A. Kribus, Analysis of potential conversion efficiency of a solar hybrid system with high-temperature stage, J. Sol. Energy Eng. 128 (2) (2005) 258–260.
[63] A. Mellor, I. Guarracino, L.F. Llin, D. Alonso-Alvarez, A. Riverola, S. Thoms, D.J. Paul, C.N. Markides, D. Chemisana, S. Maier, N. Ekins-Daukes, Specially designed solar cells for hybrid photovoltaic-thermal generators, in: 2016 IEEE 43rd Photovoltaic Specialists Conference (PVSC), 2016, pp. 2960–2963, https://doi.org/10.1109/PVSC.2016.7750203.
[64] L. Zhao, T. Detchprohm, C. Wetzel, High 400 °C operation temperature blue spectrum concentration solar junction in GaInN/GaN, Appl. Phys. Lett. 105 (24) (2014), 243903, https://doi.org/10.1063/1.4904717.
[65] X. Ren, J. Li, D. Gao, L. Wu, G. Pei, Analysis of a novel photovoltaic/thermal system using InGaN/GaN MQWs cells in high temperature applications, Renew. Energy 168 (2021) 11–20, https://doi.org/10.1016/j.renene.2020.12.035.
[66] A. Dyson, Interdisciplinary Co-development of intelligent building envelopes with on-site power generation, in: P. Sarpaneva, S. Poole (Eds.), 91st ACSA International Conference Proceedings, 2003.
[67] P. Pérez-Higueras, E.F. Fernández, High Concentrator Photovoltaics: Fundamentals, Engineering and Power Plants, Springer, 2015.
[68] A. Dyson, P.R.H. Stark, M.K. Jensen, Integrated Concentrating (IC) Solar Facade System, Department of Energy Peer Review, 2007.
[69] M. Aly Etman, N. Novelli, J. Schultz, K. Phillips, B. Andow, A. Dyson, Daylighting effect of separating direct and diffuse insolation with facade-integrated, transparent solar collector, in: Proceedings of the PLEA Conference, PLEA, Bologna, 2015.
[70] N.E. Novelli, B.C. Andow, S. Overall, C. Morse, M. Aly, Power generation and visual comfort performance of photovoltaic toplighting technologies in transient spaces, in: Proceedings of the International Building Physics Conference, IBPC, Syracuse, NY, 2018, September 26. https://surface.syr.edu/ibpc/2018/BE10/2/.
[71] N. Novelli, R. Gordon, I. Varfolomeev, Separating Direct from Diffuse: observations of visible transmittance through a tracking photovoltaic envelope, Facade Tectonics Inst. 2018 World Congress Proc. 2 (2018) 355–364.
[72] N. Novelli, J. Shultz, A. Dyson, Development of a Modeling Strategy for Adaptive Multifunctional Solar Energy Building Envelope Systems, Presented at *SimAUD*, Washington, DC, 2015.
[73] US Department of Commerce, N. (2010.). ESRL Global Monitoring Division - Global Radiation Group. Retrieved October 1, 2010, from https://www.esrl.noaa.gov/gmd/grad/solcalc/calcdetails.html.
[74] P. Zamora, P. Benítez, R. Mohedano, A. Cvetković, J. Vilaplana, Y. Li, M. Hernández, J. Chaves, J.C. Miñano, Experimental characterization of Fresnel-Köhler concentrators, J. Photon. Energy 2 (1) (2012), 021806–021806.
[75] Spectrolab, C3MJ_CCA100 Data Sheet, 2011.
[76] F. Dimroth, M. Grave, P. Beutel, U. Fiedeler, C. Karcher, T.N.D. Tibbits, et al., Wafer bonded four-junction GaInP/GaAs//GaInAsP/GaInAs concentrator solar cells with 44.7% efficiency, Prog. Photovoltaics Res. Appl. 22 (3) (2014) 277–282, https://doi.org/10.1002/pip.2475.
[77] M. Sabry, Temperature optimization of high concentrated active cooled solar cells, NRIAG J. Astron. Geophys. 5 (1) (2016) 23–29, https://doi.org/10.1016/j.nrjag.2016.03.002.
[78] H. Baig, N. Sellami, T.K. Mallick, Trapping light escaping from the edges of the optical element in a Concentrating Photovoltaic system, Energy Convers. Manag. 90 (Supplement C) (2015) 238–246, https://doi.org/10.1016/j.enconman.2014.11.026.

[79] M.A. Green, E.D. Dunlop, J. Hohl-Ebinger, M. Yoshita, N. Kopidakis, A.W.Y. Ho-Baillie, Solar cell efficiency tables (Version 55), Prog. Photovoltaics Res. Appl. 28 (1) (2020) 3–15, https://doi.org/10.1002/pip.3228.
[80] C. Schlick, An inexpensive BRDF model for physically-based rendering, Comput. Graph. Forum 13 (3) (1994) 233–246, https://doi.org/10.1111/1467-8659.1330233.
[81] Guardian Ultrawhite and Clear materials, 2015 Retrieved from https://glassanalytics.guardian.com/.aspx, July 1, 2015.
[82] G. Peharz, J.P. Ferrer Rodríguez, G. Siefer, A.W. Bett, Investigations on the temperature dependence of CPV modules equipped with triple-junction solar cells, Prog. Photovoltaics Res. Appl. 19 (1) (2011) 54–60, https://doi.org/10.1002/pip.987.